Assen Zlatarov University
Burgas, Bulgaria

ANNUAL

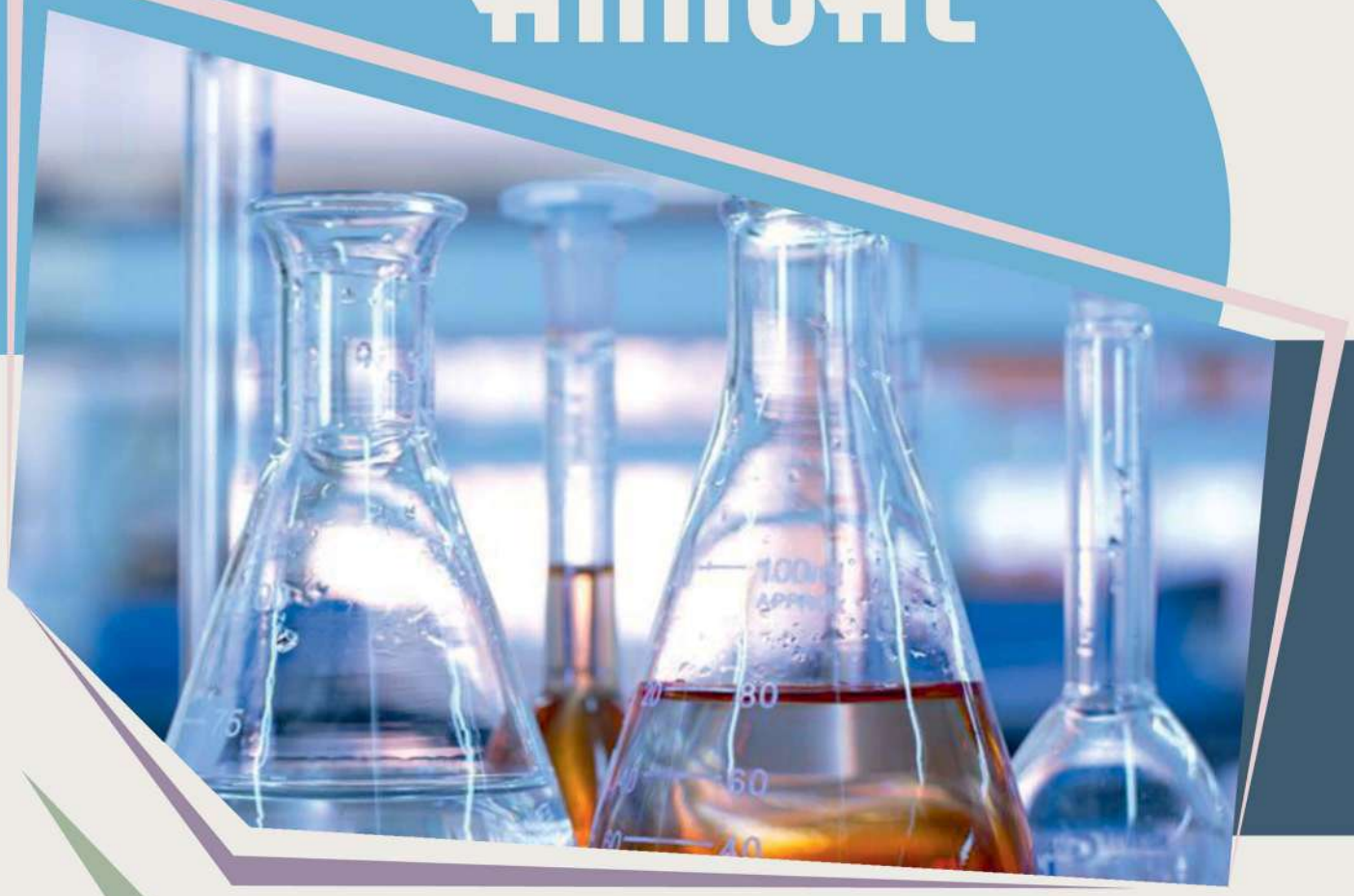

1

VOLUME LIV, BOOK 1, 2025

TECHNICAL AND NATURAL SCIENCES

ASSEN ZLATAROV UNIVERSITY
BURGAS, BULGARIA

ANNUAL

Vol. LIV, BOOK 1, 2025

TECHNICAL AND NATURAL SCIENCES

Assen Zlatarov University

Assen Zlatarov University
Annual, Vol. LIV, Book 1, 2025
Burgas 8010, Bulgaria
ISSN 2603-3968

ASSEN ZLATAROV UNIVERSITY
BURGAS, BULGARIA

ANNUAL

Annual, Vol. LIV, Book 1, 2025

TECHNICAL AND NATURAL SCIENCES

BURGAS ● 2025

VOLUME LIV (1). CONTENTS

ANNUAL OF ASSEN ZLATAROV UNIVERSITY, BURGAS
BULGARIA, 2025, v. LIV(1)

THE ROLE OF ARTIFICIAL INTELLIGENCE IN AUDITING PROCESSES AND ITS EFFECTIVENESS IN FRAUD DETECTION

Aysun Atagan Çetin
E-mail: aatagancetin@trakya.edu.tr

ABSTRACT

The rapid advancement of Artificial Intelligence (AI) has driven significant transformation across many professional fields, auditing being no exception. This paper examines the expanding role of AI in enhancing auditing processes and evaluates its effectiveness in detecting fraudulent activities Based on a comprehensive review of the existing literature, the study explores how AI technologies, including machine learning, natural language processing, and robotic process automation, are being integrated into audit methodologies to improve efficiency, accuracy, and depth analysis. The findings suggest that AI not only automates routine audit tasks and facilitates full population testing, but also shifts the fraud detection paradigm from a reactive to a proactive model by identifying subtle patterns and anomalies that are often overlooked by traditional techniques. The paper concludes by highlighting the strategic implications for the future of auditing, emphasizing the need for auditors to adapt to technological change, for educational institutions to address the emerging skills gap, and for regulatory bodies to develop robust frameworks for AI governance.

Key words: *artificial intelligence, auditing, fraud detection*

INTRODUCTION

Conceptual Framework

The contemporary business environment is characterized by unprecedented volumes of data, complex transactions, and evolving regulatory requirements. These conditions place significant pressure on the auditing profession to deliver increasingly accurate and efficient assessments. Traditional auditing methodologies, often struggle to process large datasets and detect subtle anomalies indicative of financial misstatement or fraud within compressed reporting timelines. In response to these challenges, Artificial Intelligence (AI) has emerged as a transformative force, promising to revolutionize audit practices by offering advanced analytical capabilities and automating routine tasks.

1. Core Artificial Intelligence Technologies in Auditing

The integration of Artificial Intelligence (AI) into auditing is fundamentally reshaping the profession by leveraging a suite of advanced technologies. At the heart of this transformation is Machine Learning (ML), which enables systems to learn from extensive datasets, identify complex patterns, and make informed decisions in a manner that simulates human cognition [1]. Within the audit context, ML applications are vast, ranging from the detection of fraudulent identities through predictive risk models to improvements in trading strategies and optimization of government resource management [2].

Complementing the analytical capabilities of ML, Robotic Process Automation (RPA) focuses on automating high-volume, repetitive tasks by using software robots [3]. While basic RPA handles rule-based processes, such as data entry and account reconciliation without self-improvement, more advanced applications integrate RPA with supervised learning to conduct intelligent analysis [4]. A key advantage of RPA in auditing is its ability to enable full population testing, where 100% of transactions are analyzed instead of relying on traditional sampling, thereby increasing the efficiency of identifying anomalies [3].

The third cornerstone technology is Natural Language Processing (NLP), a specialized AI branch designed to bridge the communication gap between computers and humans [1]. NLP systems are capable of parsing and analyzing vast quantities of unstructured text from sources such as invoices, contracts, and legal reports [3]. By extracting key figures, dates, and commentary, NLP can identify inconsistencies, capture critical information for risk assessment, and perform predictive analyses, such as sentiment analysis and topic

modelling, thus significantly enhancing audit efficiency and depth [5].

2. The Evolving Landscape of Financial Fraud

The growing need for advanced audit technologies is largely driven by the increasing complexity and sophistication of modern financial fraud. Firstly, fraud typologies are continuously evolving, extending beyond traditional schemes to include advanced methods such as phishing attacks, telecom fraud, and the use of generative AI to create highly realistic fake images or plagiarize scientific data, making detection by visual inspection virtually impossible [6]. This landscape also includes persistent threats such as credit card and insurance fraud, as well as misallocation of funds in the public sector, which creates opportunities for political interference [7]. The industrialization of internet-based fraud generates massive volumes of data that overwhelm traditional statistical methods [8]. Illicit activities can easily be concealed within these datasets, while the "black-box" nature of some advanced AI models can itself raise concerns about reliability and potential misinformation [9]. Consequently, traditional manual fraud detection methods are necessitating a shift toward AI-driven solutions [10].

3. AI-Driven vs. Traditional Auditing: A Methodological Comparison

The fundamental differences between AI-driven anomaly detection and traditional, rule-based auditing represent a paradigm shift in the auditing profession. The most significant distinction relates to data processing capacity and audit scope. AI systems can ingest and analyze enormous volumes of both structured and unstructured data in real time, incorporating non-traditional sources such as social media to form a holistic view [11]. This enables full population testing, in sharp contrast to traditional methods that are largely limited to manual verification of historical, structured data and rely on sampling, which inherently risks overlooking irregularities [12].

Methodologically, the approaches also differ significantly. Traditional techniques are static, using predefined rules and standardized tests to identify known issues, making them less adaptable to novel fraud schemes [13]. In contrast, AI models are dynamic; they learn from historical data to establish baseline patterns and automatically flag deviations, leveraging predictive analytics to anticipate high-risk areas before they escalate [10]. AI continuously adapts and refines its performance, uncovering hidden discrepancies that rule-based systems are likely to overlook [14]. This automation of repetitive tasks ultimately enhances audit efficiency and allows auditors to focus on higher-value strategic analysis [15].

Finally, the issue of bias and transparency presents a complex trade-off. While traditional methods are susceptible to subjective human biases in judgment and sampling [3], AI introduces new potential biases stemming from skewed training data or algorithmic assumptions [11]. Furthermore, the "black-box" nature of some complex AI models can impede transparency and accountability, creating a demand for explainable AI (XAI) tools to clarify their decision-making processes [16].

The Transformative Role of AI in Modern Auditing

1. Enhancing Core Audit Processes

Artificial intelligence fundamentally enhances core audit processes by moving beyond theoretical concepts to practical applications in risk assessment, continuous monitoring, and data analysis. Machine Learning (ML), in particular, significantly elevates the audit risk assessment process through its advanced predictive analysis, pattern recognition, and automated decision-making capabilities [17]. By processing extensive datasets, which include structured financial records, unstructured text, and even non-traditional sources such as social media behaviours, ML models can identify the likelihood of various risks, predict control failures, and provide more precise, data-driven assessments [12]. The outputs of this process include predictive models, automated decisions, and flags for deviations from normal patterns, ultimately providing auditors with objective insights that supplement their professional judgment [17].

This enhanced predictive capability is a key to enabling another significant shift: continuous auditing. Facilitated by AI, this concept transforms the audit paradigm from a retrospective, detective approach to a proactive, preventive one [18]. Instead of periodic checks, internal auditors can deploy automated scripts that consistently examine real-time data, identify irregularities, and trigger immediate notifications [19]. This model offers significant advantages over traditional reviews, including the reduction of financial losses through proactive monitoring, faster audit cycles, and the provision of real-time insights that enable preemptive interventions when financial irregularities are identified [10].

While continuous auditing reshapes the audit timeline, Robotic Process Automation (RPA) transforms the execution of routine tasks. RPA is particularly effective at automating repetitive, high-volume activities such as data entry, account reconciliation, compliance checking, and the preparation of final audit reports [3]. The primary benefits of this automation are a dramatic increase in efficiency and a reduction of manual workload, which not only minimizes human error but also enables full population testing instead of sampling [14]. This allows auditors to redirect their focus from mundane data handling to higher-level strategic analysis and decision-making, ultimately reducing audit time and costs [1].

Finally, to address the challenge of unstructured data, which constitutes a vast portion of enterprise information, auditors employ Natural Language Processing (NLP). NLP technologies are designed to parse and analyze thousands of pages of unstructured text from sources such as contracts, invoices, and even informal communication, such as emails or transcribed meetings [17]. The insights generated from this analysis are multifaceted, enabling predictive analytics such as sentiment analysis, identifying critical risks by capturing key information, and contributing to fraud detection by intercepting suspicious information within natural language sequences [5].

2. Improving Fraud Detection Effectiveness

The integration of Artificial Intelligence (AI) marks a fundamental shift in fraud detection, moving from a historically reactive posture to a more proactive and predictive approach, particularly within the public sector [20]. The core function of these technologies is centred on the detection phase of financial crime, where machine learning algorithms highlight unusual transaction patterns and suspicious account behaviours that might otherwise go unnoticed. This is powerfully demonstrated in cybersecurity auditing, where the self-learning capabilities and attack-resistant reaction mechanisms of AI enable organizations to proactively remediate risks and comply with regulations, rather than merely responding to threats after the fact [21]. This forward-looking stance is further enhanced by advancements in predictive analytics, which allow for forecasting in areas such as crime resolution, transforming the audit into a more strategic function [20].

The mechanism behind this proactive capability lies in AI's ability to identify subtle and previously unknown patterns by learning from historical data. AI systems leverage deep learning algorithms to analyze past inputs and outputs, enabling them to make accurate predictions and optimize management models in complex environments such as supply chains, effectively identifying weak links that could be exploited for fraudulent purposes [22]. While these sources confirm that AI's self-learning capacity enhances the comprehension of sophisticated threats, they primarily frame its ability to find novel patterns in terms of its outcomes, such as flagging unusual behaviour, rather than explicitly detailing the cognitive processes for uncovering schemes entirely missed by traditional methods [21].

Ultimately, AI's ability to anticipate and mitigate potential issues before they fully develop signifies its transformative impact. By performing deep learning on historical data to predict factors and identify vulnerabilities, AI directly contributes to reducing operational risk [22].

DISCUSSION

While the integration of Artificial Intelligence (AI) into auditing promises unprecedented gains in efficiency and effectiveness, its adoption is not a straightforward path. The transition is accompanied by a host of significant technical, organizational, ethical, and professional challenges that must be carefully navigated. This section discusses these critical issues, including the inherent difficulties in implementing AI, the pervasive "black box" problem that challenges professional scepticism, the key ethical dilemmas that arise, and the profound evolution of the auditor's role in an increasingly automated environment.

1. Technical and Organizational Challenges

The practical implementation of AI in auditing presents substantial technical and organizational difficulties. From a technical perspective, one of the primary challenges is the development of robust and generalizable AI models. Issues such as the need for extensive training datasets, poor model robustness in clinical or real-world applications, and a lack of generalization across different data types can impede reliability [23]. The very nature of Generative AI introduces additional risks, including the potential for data breaches, the fabrication of facts, and a fundamental lack of transparency in its decision-making processes, often referred to as the "black-box" problem [24].

The high failure rate of digital transformation projects, often due to flawed strategies or technological misfits, underscores that AI adoption must be precisely tailored to the specific needs of individual institutions rather than being a one-size-fits-all approach [20]. Organizations face the complex, multi-criteria problem of selecting the most effective AI software from numerous available options, a process fraught with uncertainty and reliance on the subjective opinions of decision experts [21]. Furthermore, the adoption of AI necessitates a broader sense of responsibility, requiring adherence to ethical and political guidelines, adjustments to organizational structure, and an expanded role for internal auditing in ensuring cybersecurity [25]. This is compounded by the complexities of legal compliance with data protection laws such as GDPR and CPRA, determining accountability for AI-driven errors, and managing the increased risks associated with opaque supply chain transactions [22].

2. The "Black-Box" Problem and Professional Scepticism

A central challenge that directly impacts the auditing profession is the "black box" nature of many advanced AI models. The inability to fully comprehend the rationale behind an AI decision poses a significant threat to an auditor's core principle of professional scepticism. This issue is acknowledged across various domains, from public sector risk management being implemented "like a black box" to the inherent opacity of Generative AI tools whose reasoning cannot be entirely trusted [25]. To maintain professional scepticism, auditors must be able to understand, question, and verify AI-driven outcomes.

In response, a strong emphasis is placed on developing Explainable AI (XAI) and other transparency-enhancing mechanisms. Proposed solutions include repurposing Generative AI to translate complex XAI outputs into coherent textual explanations and developing models that establish clear causal relationships to ensure transparent decisions [24]. Moreover, technologies such as blockchain have been suggested as tools for improving accountability by maintaining the integrity of algorithmic data and providing documented evidence of AI activities. Advanced evaluation tools are also being designed to offer more transparent, subject-level insights into model performance through interactive dashboards, helping to identify biases and data shifts [23]. These efforts are crucial for creating an auditable AI ecosystem where auditors can critically evaluate and challenge AI's outputs, thereby upholding the tenets of their profession.

3. Key Ethical Considerations

The deployment of AI in auditing introduces a complex landscape of ethical considerations, primarily centred around algorithmic bias, data privacy, and accountability. Algorithmic bias and discrimination are significant risks, as AI systems are entirely dependent on their training data and can perpetuate or even amplify existing biases, leading to inaccurate and misleading information [20]. Current evaluation frameworks are often inadequate for detecting such biases, highlighting the need for future tools to incorporate fairness-aware metrics and explainable AI [23].

Simultaneously, data privacy, confidentiality, and security become paramount. The risk of data breaches and the mismanagement of confidential information, particularly with Generative AI, has led organizations to impose strict restrictions on their use. Ensuring data security requires robust information security frameworks and policies, while solutions such as blockchain-based encryption and anonymization are proposed to ensure compliance with stringent data protection laws [21].

Finally, these challenges culminate in the overarching need for accountability and responsible AI use. The ethical dilemmas inherent in AI, termed "AI tensions", require adherence to clear guidelines and the enforcement of human authority over technological systems [25]. Establishing clear accountability mechanisms is essential to trace incorrect decisions back to their source, whether it be human misuse, developer negligence, or an external attack, ensuring that AI-driven processes align with established legal and ethical standards [24].

4. The Evolving Role of the Auditor and the Skillset Imperative

The integration of AI is set to profoundly reshape the role of the human auditor. The consensus is a definitive shift away from routine, manual tasks towards more strategic and cognitively demanding responsibilities. Automation is expected to handle repetitive work, allowing human resources to be reallocated to areas requiring critical thinking, professional judgment, and strategic analysis [20]. In this new paradigm, the auditor's role evolves into that of a strategic partner who selects and oversees AI solutions, interprets their outputs, and leverages them to gain deeper insights. In some contexts, AI may even act as a "peer-reviewer", enhancing the confidence of less

experienced professionals and improving the workflow of experts [26]. This shift is expected to reduce auditor workload and audit costs as AI enhances transparency in areas such as supply chains, potentially leading to a lower risk premium for clients [22]. This evolution necessitates a significant upskilling of the profession to fill a growing talent gap. Auditors and other professionals will require higher expertise, and enhanced skill sets to effectively engage with and manage AI tools. This includes the ability to utilize available data to find robust solutions in sophisticated audit environments and to collaborate effectively within "Lawyer-in-the-Loop" frameworks where active knowledge exchange between practitioners and AI is crucial [21]. Consequently, there is a pressing need for higher education institutions and training bodies to integrate more practical and theoretical technology-focused courses into their curricula to equip the next generation of auditors with the skills required for the AI-driven era [20].

CONCLUSION

This study synthesizes current knowledge on the transformative impact of Artificial Intelligence (AI) on the auditing profession. The review illustrates that AI represents not merely an incremental improvement but a paradigm shift, fundamentally reshaping auditors' approach to their responsibilities. By leveraging technologies, such as Machine Learning, Robotic Process Automation, and Natural Language Processing, the audit process becomes more efficient, comprehensive, and forward-looking. The capability of AI to analyze entire data populations, coupled with a transition from reactive to proactive fraud detection, signifies a substantial advancement in the ability of the profession to provide assurance and safeguard financial integrity. However, the transition to an AI-driven auditing environment is fraught with significant challenges that cannot be overlooked. The technical hurdles of developing robust models, the organizational complexities of digital transformation, and the critical ethical dilemmas surrounding bias, privacy, and accountability require careful and deliberate management. The "black-box" nature of some AI systems poses a direct challenge to the core principle of professional scepticism, necessitating a greater emphasis on Explainable AI (XAI) and robust governance frameworks. Furthermore, the evolution of the auditor's role from a procedural specialist to a strategic advisor demands significant upskilling of the profession, creating an imperative for educational and training institutions to adapt their curricula. In conclusion, the future of auditing will be characterized by a relationship between human expertise and machine intelligence. Embracing AI is no longer an option but a strategic necessity for the profession to remain relevant and effective in an increasingly complex world. Future research should move towards studies that quantify the impact of specific AI tools on audit quality and efficiency, investigate best practices for AI governance in audit firms, and explore the long-term societal implications of algorithmic assurance.

REFERENCES

1. Aldemir, C., Uçma Uysal, T. AI Competencies for Internal Auditors in the Public Sector. EDPACS, 2024, 69(1), pp. 3–21.
2. Anomah, S., Ayeboafo, B., Owusu, A., Aduamoah, M. Adapting to AI: exploring the implications of AI integration in shaping the accounting and auditing profession for developing economies. EDPACS, 2024, 69(11), pp. 28–52.
3. Murikah, W., Nthenge, J. K., Musyoka, F. M. Bias and ethics of AI systems applied in auditing - A systematic review. Scientific African, 2024, 25, e02281.
4. Wang, S., Lim, X., Duerden, R., Whittaker, J., Oliveira, P. 31 AI evaluation of tumour content and histology sample quality with change in needle type used in Image Guided Lung Biopsy: a retrospective audit. Lung Cancer, 2025, 200, 108142.
5. Liao, F.-n., Zhang, C., Zhang, J.-j., Yan, X., Chen, T.-x. Hyperbole or reality? The effect of auditors' AI education on audit report timeliness. International Review of Financial Analysis, 2024, 91, 103050.
6. Gu, J., Wang, X., Li, C., Zhao, J., Fu, W., Liang, G., Qiu, J. AI-enabled image fraud in scientific publications. Patterns (N Y), 2022, 3(7), 100511.
7. Fajardo, B., Neiva, S. 'Malha Fina de Convênios': an AI application for auditing in the Brazilian federal government. Public Money & Management, 2025, 1-12.
8. Wanga, Z., Shenb, Q., Bic, S., Fu, C. AI Empowers Data Mining Models for Financial Fraud Detection and Prevention Systems. Procedia Computer Science, 2024, 243, pp. 891–899.

9. Herbosch, M. Fraud by generative AI chatbots: On the thin line between deception and negligence. Computer Law & Security Review, 2024, 52, 105941.
10. Bouchetara, M., Zerouti, M., Zouambi, A. R. Leveraging Artificial Intelligence (AI) in Public Sector Financial Risk Management: Innovations, Challenges, And Future Directions. EDPACS, 2024, 69(9), pp. 124–144.
11. Li, Y., & Goel, S. Bridging IT auditors and AI auditing: Understanding pathways to effective IT audits of AI-driven processes. Advances in Accounting, 2025, 69, 100842.
12. Shivram, V. Auditing with AI: A Theoretical Framework for Applying Machine Learning Across the Internal Audit Lifecycle. EDPACS, 2024, 69(1), pp. 22–40.
13. Özbaltan, N. Applying Machine Learning to Audit Data: Enhancing Fraud Detection, Risk Assessment and Audit Efficiency. EDPACS, 2024, 69(9), pp. 70–86.
14. Bin-Nashwan, S. A., Li, J. Z., Jiang, H., Bajary, A. R., Ma'aji, M. M. Does AI adoption redefine financial reporting accuracy, auditing efficiency, and information asymmetry? An integrated model of TOE-TAM-RDT and big data governance. Computers in Human Behavior Reports, 2025, 17, 100572.
15. Damar, M., Aydın, Ö., Nihal Cagle, M., Özoğuz, E., Ömer Köse, H., Özen, A. Navigating the digital frontier: transformative technologies reshaping public administration. EDPACS, 2024, 69(9), pp. 41–69.
16. Laine, J., Minkkinen, M., Mäntymäki, M. Ethics-based AI auditing: A systematic literature review on conceptualizations of ethical principles and knowledge contributions to stakeholders. Information & Management, 2024, 61(5), 103969.
17. Graves, M., Ratti, E. A capability approach to ethical development and internal auditing of AI technology. Journal of Responsible Technology, 2025, 22, 100121.
18. Waltersdorfer, L., Sabou, M. Leveraging Knowledge Graphs for AI System Auditing and Transparency. Journal of Web Semantics, 2025, 84, 100849.
19. Taşdöken, Ö. Use of Artificial Intelligence and Audit Analytics in Internal Audit Processes in The Public Sector. EDPACS, 2024, 69(9), pp. 1–15.
20. Damar, M., Aydın, Ö., Özoğuz, E., Aydın, Ü., Özen, A. Turkish Court of Accounts: Analyzing Financial Audit, Digitalization, AI Impact. EDPACS, 2024, 69(9), pp. 16–40.
21. Sahin, F., Menekse, A., Yilmaz, S. AI software selection for cybersecurity auditing using neutrosophic CRITIC CODAS. Applied Soft Computing, 2025, 179, 113295.
22. Wang, J., Zhao, M., Huang, X., Song, Z., Sun, D. Supply chain diffusion mechanisms for AI applications: A perspective on audit pricing. International Review of Financial Analysis, 2024, 93, 103113.
23. Aumente-Maestro, C., Muller, M., Remeseiro, B., Diez, J., Reyes, M. AUDIT: An open-source Python library for AI model evaluation with use cases in MRI brain tumor segmentation. Comput Methods Programs Biomed, 2025, 271, 108991.
24. Sachan, S., Liu, X. Blockchain-based auditing of legal decisions supported by explainable AI and generative AI tools. Engineering Applications of Artificial Intelligence, 2024, 129, 107666.
25. Güney, C., Ala, T. The Insights of Publications in the Field of Artificial Intelligence (AI)-Based Risk Management in Public Sector: A Bibliometric Overview. EDPACS, 2024, 69(1), pp. 41–68.
26. Yaqub, M., Sleep, N., Syme, S., Chen, Z., Ryou, H., Walton, S., Papageorghiou, A. T. 491 ScanNav® audit: an AI-powered screening assistant for fetal anatomical ultrasound. American Journal of Obstetrics and Gynecology, 2021, 224(2).

ANNUAL OF ASSEN ZLATAROV UNIVERSITY, BURGAS
BULGARIA, 2025, v. LIV(1)

IDENTIFICATION OF THE MAIN AIR POLLUTION HOTSPOTS IN THE CITY OF BURGAS

Denitza Petrova, Viktoria Yaneva, Bozhidar Stavrev, Stela Naydenova, Nikola Todorov
E-mail: nikola_todorov@btu.bg

ABSTRACT

Air pollution hotspots are specific urban zones where pollutant levels markedly exceed those of adjacent areas. Identifying the principal hotspots is essential for improving overall air quality and protecting public health. In this study, we have considered: the levels of pollutants most harmful to human health (particulate matter, nitrogen dioxide, sulphur dioxide and tropospheric ozone); noise pollution and road traffic (the dominant urban source of air pollution); topographic and meteorological characteristics and the number of exposed individuals. Based on these factors, ten hotspots were identified in Burgas for future monitoring and health-risk assessment.

Keywords: *monitoring; traffic air pollution; noise exposure; health*

INTRODUCTION

Clean air is vital for human survival and well-being, yet it is increasingly scarce in the contemporary urban environment. Air pollution is regarded as the greatest environmental health risk globally, contributing to approximately 6.7 million premature deaths per year, according to the World Health Organization (WHO). Urban populations are particularly vulnerable. Particulate matter, nitrogen dioxide and tropospheric ozone account for most of these premature deaths [1, 2]. According to the Organisation for Economic Co-operation and Development (OECD), by 2050 air pollution is expected to become the leading environmental cause of mortality worldwide, surpassing the lack of clean water and poor sanitation [3]. The evidence of adverse health effects from exposure to polluted air is robust, although there are still knowledge gaps regarding the precise mechanisms by which pollutants affect human health [4].

Major sources of ambient air pollution include transport, heavy industry (including power generation), light industry, households and agriculture. Although road transport has been developing in recent years towards reducing emissions, in large cities it remains the main factor for air pollution, due to the increase of people and vehicles.

The steady growth in road transport and the centralization of household heating have made traffic the most important source of urban air pollution. Fuel consumption and emissions on a road segment increase substantially under stop-and-go conditions [5, 6]. Consequently, total PM10 and PM2.5 emissions near traffic lights, bus stops and congestion-related stops are consistently several times higher than on uncongested segments [7–9].

Pollutant concentration in an urban street can be expressed as the sum of background and street-level contributions:

$$C = cb + cs,$$

where **C** is the street-level concentration; cb is the urban background and cs is the contribution of traffic on the street itself.

Higher concentrations imply higher exposure and health risk for people walking or cycling along streets, waiting at bus stops, or traveling by passenger car, motorcycle, heavy-duty vehicle, or bus [10, 11]. Numerous studies confirm that commuting substantially contributes to personal exposure: up to 30% of the daily inhaled dose of black carbon (BC) and ~12% of daily PM2.5 exposure may occur during commuting, although commuting time constitutes no more than ~6% of the day [12].

Short-term exposure to elevated concentrations in Air pollution hotspots can significantly impact health [13–15], especially for individuals whose work requires prolonged stays in such environments.

There is no universally accepted methodology for defining and delineating hotspots. Air quality monitoring stations (AQMS) provide valuable information but are expensive and cannot be positioned in the hotspots. Researchers often identify such points based on source activity (e.g. high

traffic density), but urban morphology and atmospheric conditions must also be considered. Poor dispersion, such as stagnant air or temperature inversions, can lead to pollutant accumulation and hotspot formation.

We have found no prior literature on identifying hotspots in Burgas. Their identification is of great importance for: (i) targeted policy development and effective resource allocation; (ii) enabling individuals to reduce personal exposure during mobility; (iii) public-health actions-targeted advisories for sensitive groups, such as children, older adults and persons with pre-existing respiratory or cardiovascular disease; (iv) better understanding of pollutant-specific health effects and developing prevention strategies and (v) reducing risk exposure (e.g., guidance for outdoor activities on high-pollution days, or recommendations for air-purifier use).

The aim of this work is to identify the main air pollution hotspots in Burgas based on: AQMS data on air pollution; noise and traffic; topographic and meteorological factors and the number of exposed individuals.

METHODS

Object of the study

The study area is the city of Burgas, the largest city in Southeastern Bulgaria and the second largest on the Bulgarian Black Sea coast. With an area of 253.644 km², it is among the country's largest cities. According to NSI, the population is 189,014 (31 December 2024).

By virtue of its geographic position, the municipality occupies an important place in Bulgaria's transport and communication system. Key transport corridors traverse it in the east-west direction, with connections to both northern and southern Bulgaria.

In Burgas an integrated transport-communication system has been established. Transport services are provided by buses, taxis and cargo vehicles, as well as private and company motor vehicles. As in most cities, light automobiles (up to 3.5 tonnes) predominate. According to Burgas Municipality, in 2022 Burgas had over 200,000 cars, increasing by ~1,500 annually.

Measurement of Air pollution levels

In Burgas, air pollution is continuously measured at seven points [16]: AQMS "Dolno Ezerovo" (AQMS DE); AQMS "Meden Rudnik" (AQMS MR); Differential Optical Automatic System (DOAS) OPSIS Burgas; AQMS "Slaveykov" (AQMS S); AQMS City Center (AQMS CC); AQMS "Lazur" (AQMS L) and Mobile Air Quality Station (MAQMS) of Burgas Municipality. The mobile station allows measurements at different locations across the territory of the city.

Measurement of noise pollution

The noise-monitoring program in Burgas includes 37 observation points. The analysis concerns daytime noise (L_day) from 8:00 to 17:30. L_day values were determined instrumentally using an integrating sound-level meter, type 2238 B&K, ID No. 2414737, Class I, SC No. 003-IAV/10.01.2019 and a sound calibrator type 4231, ID No. 2517985, SC No. 002-IAV/10.01.2019 [17].

RESULTS AND DISCUSSION

Air pollution hotspots

Air pollution hotspots are localized urban zones where pollutant levels are significantly higher than in adjacent areas.

Background air pollution refers to the presence of pollutants in the air in non-urban areas. Those pollutants are persistent and widespread, occurring as a result of various natural and human activities. In urban environments, air pollution is higher. In some zones, transport, household, commercial and industrial activities can elevate concentrations well above background levels. Figure 1 schematically contrasts non-urban, urban and hotspot levels.

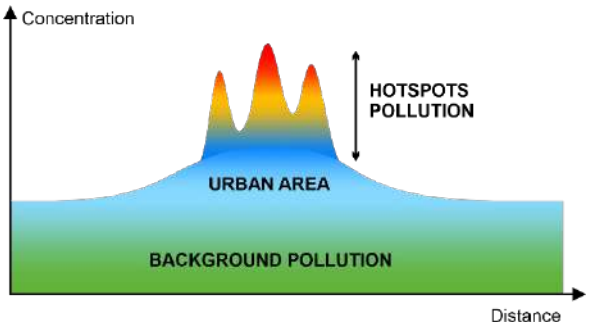

Fig. 1. Schematic illustration of air pollution

Air pollution from particulate matter, nitrogen dioxide, sulphur dioxide and tropospheric ozone

WHO identifies particulate matter (PM), nitrogen dioxide (NO_2), sulphur dioxide (SO_2), and tropospheric ozone (O_3) as pollutants most harmful to human health.

In Burgas, PM10 is monitored at seven automatic stations, while PM2.5 is monitored at three. Table 1 reports annual average values (AAV) of PM10 and PM2.5 for 2024 [18].

Table 1. Annual average values (AAV) and number of exceedances of the daily limit (NEDL) of PM10 and PM2.5 in 2024

Monitoring Point	PM10		PM2.5
	AAV, μg/m^3	NEDL	AAV, μg/m^3
AQMS DE	27.67	18	–
AQMS MR	18.05	9	–
DOAS OPSIS	24.51	4	–
AQMS S	23.65	12	–
AQMS CC	21.77	5	7.34
AQMS L	19.06	1	10.42
M AQMS	21.1	0	11.22

For PM10 AAV, the highest level is at AQMS "Dolno Ezerovo," followed by DOAS OPSIS and AQMS "Slaveykov." The highest PM2.5 AAV was recorded by the Mobile AQ station, which can be explained by its easy positioning in higher-pollution areas.

NO_2, SO_2 and O_3 are monitored at three points: AQMS "Dolno Ezerovo," AQMS "Meden Rudnik," and DOAS OPSIS within the National Monitoring System. The Mobile AQ station provides additional measurements. Table 2 presents AAV, maximum daily-mean values (DMV) and highest hourly-mean values (HMV) for NO_2, SO_2, PM10 and O_3 air pollution in 2024.

Table 2. AAV, maximum DMV and highest HMV of NO_2, SO_2, PM10 and O_3 in Burgas (2024)

Monitoring Point	Pollutant	AAV, μg/m3	Max daily mean value, μg/m3	Highest recorded hourly mean value, μg/m3
AQMS DE	NO_2	12.1	34.40	66.72
	SO_2	16.7	47.50	107.19
	PM10	27.67	89.73	186.63
	O_3	55.25	108.26	158.25
AQMS MR	NO_2	16.19	31.08	73.86
	SO_2	17.27	30.62	87.13
	PM10	18.05	74.45	–
	O_3	56.87	102,50	176.13
DOAS OPSIS	NO_2	25.77	62.11	121.39
	SO_2	3.99	26.23	87.55
	PM10	24.51	68.30	–
	O_3	59.87	98.60	151.72

For NO_2, AAV maximum DMV and HMV are highest at DOAS OPSIS, plausibly due to its proximity to Stefan Stambolov Blvd., which has the highest intensity of car traffic in Burgas. All recorded values for NO_2 pollution are lower than the relevant standards [19], but the following should be considered: NO_2 is heavier than air and vertical homogeneity is difficult to achieve, thus concentrations measured at 0.6 m (children's breathing zone), 1.5 m (adults) and 2–15 m (typical AQMS inlet heights, including DOAS OPSIS in Burgas) may differ substantially [20].

Air pollution from SO_2 at AQMS "Meden Rudnik" and AQMS "Dolno Ezerovo" exceed those at DOAS OPSIS. This is due to a couple of reasons: the proximity of LUKOIL Neftochim Burgas AD, the lack of central heating and the presence of many family houses using mainly solid fuel for heating.

Air pollution from anthropogenic Ozone shows no substantial differences in the three points.

Noise pollution

In cities, noise pollution is primarily due to motor traffic. Transport-noise monitoring in Burgas identified 14 points impacted by intense road traffic. The average sound-pressure levels in 2024 ranged from 65 to 73 dB(A) at the following points [17]:

- Stefan Stambolov Blvd., Zornitsa complex in front of bl. 2–3: 72 dB(A)
- Stefan Stambolov Blvd., bl. 43: 70 dB(A)
- Professor Yakimov Blvd., in front of Burgas State University Prof. Dr. Assen Zlatarov: 70 dB(A)
- Maria Luiza Blvd., bl. 1: 69 dB(A)
- D. Dimov Blvd., bl. 55: 65 dB(A)
- Slaveykov complex, Stefan Stambolov Blvd., bl. 95: 71 dB(A)
- Struga Blvd., in front of bl. 92: 73 dB(A)
- Bulair St., near Bulair Hotel: 71 dB(A)
- San Stefano Blvd., bl. 105: 71 dB(A)
- Demokratsia Blvd., bl. 77: 71 dB(A)
- Hristo Botev Blvd., bl. 59: 72 dB(A)
- Ivan Vazov Blvd., Seasons Hotel: 72 dB(A)
- Nikola Petkov Blvd., bl. 18: 71 dB(A)
- Meden Rudnik complex, Zahari Stoyanov Blvd., opposite bl. 410: 71 dB(A)

These levels are 5–13 dB(A) above the limit value [21].

The main noise sources are:

- high traffic intensity, especially during peak hours;

- construction works in residential, commercial and industrial areas;
- minimal building-to-roadway distances.

The average hourly traffic intensity across this group is high: 1,546 to 3,657 vehicles/hour-peaking in Stefan Stambolov Blvd., Zornitsa (3,657 vehicles/hour) and lowest in D. Dimov Blvd., bl. 55 (1,546 vehicles/hour). The average equivalent noise level in 2024 was 71 dB(A) (limit: 60 dB(A)), with mean hourly traffic intensity of 2,302.43 vehicles/hour.

Identification of the main air pollution hotspots

To identify air pollution hotspots, the following factors were studied:

- Air pollution levels of PM, NO_2, SO_2 and O_3 (WHO-listed as most harmful to health);
- Noise pollution exceeding 60 dB(A) on boulevards and streets in the city due to high traffic intensity;
- Topographic and meteorological characteristics (humidity, inversion, etc.) conducive to pollutant accumulation;
- Number of exposed individuals (children and adults) in the respective zones.

On this basis, the following principal air pollution hotspots in Burgas were identified:

- Prof. Yakim Yakimov Blvd. No. 1 (entrance of Burgas State University),
- Yanko Komitov Blvd., traffic lights at Mall Galleria,
- Stefan Stambolov Blvd. No. 50, Okruzhna Bolnitsa bus stop,
- Stefan Stambolov Blvd. No. 69 and Dunav St., intersection near the Vocational High School of Mechatronics and Electronics,
- Stefan Stambolov Blvd. and San Stefano Blvd., intersection near the New Post Office,
- Demokratsia Blvd. and Gen. Gurko St., intersection near Diagnostic-Consultancy Center 2 Burgas,
- Hristo Botev St., NHK bus stop,
- Ivan Vazov Blvd., Aleksandrovska St. and Tsaritsa Yoanna Sq. intersection,
- Dame Gruev Blvd. and Struga Blvd. intersection,
- Demokratsia Blvd., Demokratsia bus stop.

These points will be subject to subsequent monitoring and health-risk assessment.

CONCLUSION

Identifying urban Air pollution hotspots requires understanding of the interacting factors that create and sustain them. To identify hotspots, air pollution with particulate matter, nitrogen dioxide, sulphur dioxide and ozone was studied. The results showed that all values were lower than the regulatory standards. By contrast, noise assessments revealed fourteen zones exceeding the limits by 5–13 dB(A), driven by road traffic, the dominant urban source of pollution. Based on these and on specific topographic and meteorological conditions, ten principal hotspots were identified for targeted monitoring and health-risk assessment.

REFERENCES

1. World Health Organization (WHO) Air Quality and Health, 2014 Fact Sheet N°313. Updated September 2016.
2. European Environment Agency (EEA) How air pollution affects our health, Europe, 2025
3. Organization for Economic Co-Operation and Development (OECD) Environmental Outlook to 2050: The Consequences of Inaction. Organization for Economic Co-Operation and Development (OECD); Paris, France: 2012.
4. Jianwei, Zhang; Zhao, Chen; Dan, Shan; Yang, Wu; Yue, Zhao; Chen, Li; Yue, Shu; Xiaoyu, Linghu; Baiqi, Wang, Adverse effects of exposure to fine particles and ultrafine particles in the environment on different organs of organisms, Journal of Environmental Sciences, 2024, 135, pp. 449–473.
5. Choudhary A., Gokhale S., On-road measurements and modelling of vehicular emissions during traffic interruption and congestion events in an urban traffic corridor, Atmos. Pollut. Res., 2019, 10, pp. 480–492.
6. Rakha H.A., Ding Y., Impact of Stops on Vehicle Fuel Consumption and Emissions. J. Transp. Eng., 2003, 129, pp. 23–32.
7. Yu Q, Lu L, Li T, Tu R., Quantifying the Impact of Alternative Bus Stop Platforms on Vehicle Emissions and Individual Pollution Exposure at Bus Stops. Int J Environ Res Public Health, 2022, 27, pp. 6552.
8. Yu Q., Li T., Evaluation of bus emissions generated near bus stops. Atmos. Environ., 2014, 85, pp. 195–203.
9. Moore A., Figliozzi M., Monsere M., Bus stop air quality: An empirical analysis of exposure

to particulate matter at bus stop shelters, Proceedings of the 91st Transportation Research Board Annual Meeting, 2012.
10. Otto Hänninen, Heli Lehtomäki, Antti Korhonen, Tuukka Kokkola, Anni Hartikainen, Olli Sippula, Ulla Haverinen-Shaughnessy, Pekka Leviäkangas, Isabell Katharina Rumrich, Health risks related to air pollution by transport categories and vehicle types: Comparison by mortality indicators, Environment International, 2025, 202, 109657.
11. Shen J., Gao Z., Commuter exposure to particulate matters in four common transportation modes in Nanjing, Build. Environ., 2019, 156, pp. 156–170.
12. Samuele Marinello, F. Lolli, Antonio Maria Coruzzolo, Rita Gamberini, Exposure to Air Pollution in Transport Microenvironments, Sustainability, 2023, 15(15), 11958.
13. Le, H. T. K., & Poom, A. Advancing environmental exposure and health impact assessment research with travel behaviour studies, Transport Reviews, 2023, 44, pp. 733–742.
14. Chaix, B., Mobile sensing in environmental health and neighborhood research, Annual Review of Public Health, 2018, 39, pp. 367–384.
15. Mitsakou, C., Adamson, J.P., Doutsi, A., Brunt, H., Jones, S.J., Gowers, A.M., Exley, S., Assessing the Exposure to Air Pollution during Transport in Urban Areas - Evidence Review, J. Transp. Health, 2021, 21, 101064.
16. Regional inspectorate for the environment and waters Burgas, Regional report on the state of the environment 2023 Burgas, 2024.
17. Hadzhiliev V. Report with analysis and assessment of noise pollution in the monitored settlements, Regional Health Inspectorate, Burgas, 2024.
18. Burgas Municipality. Report on the implementation of the Program for Improving the Quality of Atmospheric Air for the period 1.01.2024 to 31.01.2024. Burgas 2024.
19. Regulation No. 12 of July 15, 2010 on standards for sulfur dioxide, nitrogen dioxide, fine particulate matter (PM), lead, benzene, carbon monoxide and ozone in ambient air. Ministry of Environment and Health, Sofia.2010.
20. Restrepo, C., R. Zimmerman, G. Thurst et al., A comparison of ground-level air quality data with New York State Department of Environmental Conservation monitoring stations data in South Bronx, New York. Atmos. Environ., 2004, 38(31) pp. 5295–5304.
21. Regulation no. 6 of 2006 on noise indicators in the environment, State Gazette No. 24 of 25 March 2022.

ANNUAL OF ASSEN ZLATAROV UNIVERSITY, BURGAS
BULGARIA, 2025, v. LIV(1)

EFFECT OF METFORMIN ON RENAL FUNCTION IN PATIENTS WITH TYPE 2 DIABETES: A RETROSPECTIVE SINGLE-CENTRE OBSERVATION IN OUTPATIENT PRACTICE

Nikolay Kostadinov
E-mail: n.kostadinov_m.d@abv.bg

ABSTRACT

Diabetic kidney disease (DND) is a leading cause of chronic kidney failure in patients with type 2 diabetes mellitus (T2DM). Metformin is the standard first-line therapy, known for its glucose-lowering properties and evidence of its renoprotective effect. The present retrospective single-centre study included 130 outpatients in Bulgaria, divided into two groups: 65 patients treated with metformin for ≥1 year and 65 not receiving metformin.

The primary endpoints were doubling of serum creatinine, reduction of eGFR to ≤15 mL/min/1.73 m², and progression of chronic kidney disease (CKD). Secondary endpoints included mean change in eGFR, development of microalbuminuria, and change in HbA1c.

Patients treated with metformin demonstrated a better preserved renal function, with a lower frequency of serum creatinine doubling and decrease of eGFR, fewer cases of CKD progression and a significantly lower frequency of microalbuminuria (18.5% vs. 38.5%, p=0.015). HbA1c control was also better (-0.6% vs -0.2%, p=0.002).

The results confirm the renoprotective effect of metformin in outpatients with T2DM and support its inclusion in the therapeutic regimens for long-term renal protection.

Key words: *metformin, type 2 diabetes mellitus, renal function*

INTRODUCTION

Diabetic kidney disease (DRD) is a leading cause of chronic renal failure and significantly increases the risk of cardiovascular events and mortality in patients with type 2 diabetes mellitus (T2DM) [1]. Metformin is a first-line therapy in T2DM, known for its glucose-lowering properties and favourable safety profile.

In recent years, accumulating evidence has support the renoprotective effect of metformin. Published analyses indicate that patients treated with metformin experience a slower decline in renal function. Mechanisms include reduction of oxidative stress, anti-inflammatory effects, improvement of metabolic profile and activation of the adenosine monophosphate-activated protein kinase (AMPK) pathway, which plays a key role in the protection of renal cells in hyperglycaemia and proteinuria [2, 3]. Metformin exhibits pleiotropic effects that go beyond its antihyperglycaemic effect, with a number of observational studies suggesting that its use is associated with lower overall mortality in patients with chronic kidney disease (CKD) [4].

Despite extensive international data, the available evidence for the Bulgarian population in ambulatory settings remains limited. Most studies have been conducted in hospital environments or among populations with different ethnic and therapeutic characteristics, which limits the applicability of the findings to real practice in this country. As the majority of T2D patients are followed on an outpatient basis, assessment of the effect of metformin on renal function in this setting is of key importance for the prevention of diabetic nephropathy. The present study aims to evaluate the impact of metformin therapy on renal function indicators in T2D patients followed in outpatient practice in Bulgaria, providing data relevant to daily clinical care.

OBJECTIVE

To assess the renoprotective effect of metformin in patients with type 2 diabetes mellitus followed in an outpatient setting by analysing changes in renal function over a nine-month follow-up period.

MATERIAL AND METHODS

This retrospective single-centre observational study included 130 patients with T2DM followed in an outpatient endocrinology practice in the city of Burgas between November 2022 and July 2023. Patients were divided into two groups: those receiving long-term metformin therapy (≥1 year) of optimally tolerated doses (M group) and those not treated with metformin (NM group). Age, sex, baseline serum creatinine, glomerular filtration rate (eGFR), microalbuminuria (MALB) and glycated haemoglobin (HbA1c) were analysed. Primary endpoints: doubling of serum creatinine, eGFR≤15mL/min/1.73m^2 and development or exacerbation of CKD.

Patients were divided into two study groups:

• Group M (metformin): n=65, long-term metformin use ≥1 year;

• Group NM (non-metformin): n=65, treated with other antidiabetic drugs.

Participants in the present study were included based on the following predefined criteria:

Inclusion criteria:

• Confirmed diagnosis of DM2T with treatment duration ≥12 months

• Availability of renal function data (eGFR and serum creatinine)

• Follow-up period: 9 months.

Subjects who met any of the following conditions were excluded from the analysis:

Exclusion criteria:

• Initial eGFR <30 mL/min/1.73 m², i.e. severe CKD (stage 4 or 5)]

• History of acute kidney injury within the preceding 12 months.

• Use of nephrotoxic medications (e.g. nonsteroidal anti-inflammatory drugs, chemotherapeutic agents, or contrast media) that could independently affect renal function.

Criteria rationale:

As already stated, the present observational retrospective study aimed to evaluate the renoprotective effect of metformin in patients with T2DM. Clearly defined inclusion and exclusion criteria were applied in sampling to ensure population homogeneity and minimize confounding factors affecting renal function. The requirement for a confirmed diagnosis of T2DM and treatment for a period of at least 12 months was intended to ensure the inclusion of patients with an established and stable metabolic status, avoiding variations related to early stages of therapy or diagnosis. The inclusion of only patients with tracked eGFR and serum creatinine values at least once a year allowed a reliable and real assessment of the dynamics of renal function. Patients with baseline eGFR <30 mL/min/1.73 m^2 were excluded because at this stage of chronic kidney disease (CKD) metformin is contraindicated due to an increased risk of lactic acidosis. Inclusion of similar patients would compromise the internal validity of the analysis and make the direct comparison between the groups difficult. Exclusion of patients with acute kidney injury in the previous 12 months was motivated by the risk of transient and uncharacteristic changes in renal function that do not reflect the long-term progression of CKD. Similarly, patients with known use of nephrotoxic medications were also excluded to limit the influence of external factors capable of causing renal damage regardless of metabolic control or therapeutic regimen.

Estimated glomerular filtration rate (eGFR) was used to assess renal function using the 2021 CKD-EPI (Chronic Kidney Disease Epidemiology Collaboration) formula, validated for a wide range of patients and providing higher accuracy than traditional methods [5].

By applying these criteria, greater homogeneity of the study population and high clinical relevance of the results was achieved.

The main (primary) endpoints (Table 1a) in the present study included objective markers of renal function deterioration as follows:

• Doubling of serum creatinine (≥100% from baseline);

• Reduction of eGFR to ≤15 mL/min/1.73 m^2;

• Progression of CKD requiring hospitalization, dialysis or transplantation;

Additional indicators (Table 1b) for the assessment of renal and metabolic dynamics include:

Secondary endpoints:

• Mean change in eGFR;

• Development of microalbuminuria (MALB >30 mg/L);

• Change in HbA1c (%).

Statistical analysis

Data were processed and analysed using IBM SPSS Statistics version 22.0. A multivariate regression model adjusted for potential confounding variables such as age, sex, baseline renal function, glycaemic control and comorbidities was used to examine the associations between metformin therapy and renal function in patients. To compare the means between the two independent groups, patients treated with metformin (M) and those without metformin therapy(NM), an Independent

Samples T-test was applied. Statistical significance was established at a confidence level of $p<0.05$. When interpreting the results, the effects of age, srx, glycated haemoglobin, presence of microalbuminuria, comorbidities, and baseline renal function were taken into account.

Table 1. Definition of primary and secondary endpoints

(a) Primary endpoints	**Definition:**
Doubling of serum creatinine	An increase in serum creatinine of ≥100% from baseline
Decrease in eGFR to ≤15 mL/min/1.73 m^2	Recorded eGFR value ≤15 mL/min/1.73 m^2, calculated using the 2021 CKD-EPI formula
Progression of CKD requiring hospitalization	Diagnosis and hospitalization due to deterioration of renal function, dialysis or transplantation
b) Secondary endpoints	**Definition:**
Mean change in eGFR	Difference between eGFR at baseline and end of follow-up period (mL/min/1.73 m^2)
Development of microalbuminuria	Increased MALB relative to reference value (>30 mg/L)
Change in glycated haemoglobin (HbA1c)	Difference between HbA1c values at inclusion and at the end of follow-up (%)

RESULTS

Table 2 presents the main demographic and clinical parameters of the two groups of patients who were comparable in terms of age, sex, HbA1c, microalbuminuria, comorbidities and baseline renal function ($p > 0.05$).

• Total number of patients: 130 (65 M, 65 NM);

• Average age: 62.4 ± 8.1 (M) vs 63.1 ± 7.9 (NM);

• Comorbidities, HbA1c, eGFR and microalbuminuria: comparable between groups ($p > 0.05$).

Key findings:

• Better renal function in the metformin group;

• Lower frequency of doubling of serum creatinine and decrease in eGFR ≤15 mL/min/1.73 m^2;

• Progression of CKD with hospitalization: 2 cases (M) vs 7 cases (NM);

• Mean eGFR values better preserved in the M group;

• Microalbuminuria: 18.5% (M) vs 38.5% (NM);

• HbA1c: more significant reduction in group M.

Better renal function was observed in T2T patients treated with metformin compared to patients not taking metformin. In particular, the metformin group showed a lower frequency of doubling of serum creatinine and fewer cases with a decrease in eGFR to ≤15 mL/min/1.73 m^2. Also, progression of chronic kidney disease requiring hospitalization was less frequent in metformin patients. Mean eGFR values were better preserved in the metformin group, and the incidence of microalbuminuria was lower compared to the control group. In addition, better control of glycated haemoglobin (HbA1c) was observed in metformin patients, which contributed to the delay of kidney damage (Table 3).

Table 2. Main characteristics of the patients

Parameter	**Group M (n=65)**	**Group NM (n=65)**	***p*-value**
Average age (years)	62.4 ± 8.1	63.1 ± 7.9	0.58
Sex (male/female)	34 / 31	36 / 29	0.68
Duration of ZD2T (years)	8.5 ± 3.2	8.7 ± 3.5	0.74
Glycated haemoglobin (HbA1c, %)	7.4 ± 0.6	7.5 ± 0.7	0.48
Microalbuminuria (MALB >30 mg/L)	18 (27.7%)	21 (32.3%)	0.53
Concomitant diseases:			
Arterial hypertension (%)	43 (66.2%)	45 (69.2%)	0.68

Coronary artery disease (%)	21 (32.3%)	19 (29.2%)	0.69
Creatinine (μmol/L)	85.2 ± 9.8	87.6 ± 10.3	0.23
Glomerular filtration rate (eGFR, mL/min/1.73 m^2)	89.1 ± 2.5	86.5 ± 3.1	0.25

Table 3. Results of primary endpoints

End point	Group M (start/ finish)	Group NM (start/ finish)
Doubling of serum creatinine (%)	0/5	0/15
eGFR (mL/min/1.73 m^2)	89.1±2.5/ 87.2±2.1	86.5±3.1/ 80.7±3.7
eGFR ≤15 mL/min/1.73 m^2 (number of patients)	0/1	0/4
Progression of CKD with hospitalization	0/2	0/7
HbA1c (%)	7.4±0.6/ 6.8±0.4	7.5±0.7/ 7.3±0.5

The results of the secondary endpoints showed that patients in the metformin-treated group had a significantly smaller decline in renal function, as measured by mean change in eGFR, compared to patients without metformin therapy ($p < 0.001$). Furthermore, the development of microalbuminuria was lower in the metformin group (18.5% (M) vs. 38.5% (NM), p=0.015). Glycated haemoglobin control was also better in metformin patients, with a greater reduction in HbA1c ($p = 0.002$). These results further support the potential renoprotective effect of metformin in T2D patients (Table 4).

Table 4. Results of secondary endpoints

Indicator	Group M (n=65)	Group NM (n=65)	*p*-value
Mean change in eGFR (mL/min/ 1.73 m^2)	–1.9± 3.4	–5.8± 4.7	<0.001
Development of microalbuminuria (%)	12 (18.5%)	25 (38.5%)	0.015
Change in HbA1c (%)	–0.6 ± 0.4	-0.2 ± 0.5	0.002

Interpretation of results:

• Data support the renoprotective effect of metformin in outpatients with T2DM;

• Better glycaemic control further contributes to the delay of the progression of kidney damage.

DISCUSSION

The findings of the present study support the growing evidence for the renoprotective effect of metformin in patients with type 2 diabetes mellitus (T2DM) [6]. Metformin therapy was associated with a significantly lower risk of progressive deterioration of renal function in the outpatient setting, consistent with the results of large cohort studies and meta-analyses [7].

Our observation shows that metformin slows the progression of chronic kidney disease (CKD) and reduces the incidence of microalbuminuria, providing long-term protection of the renal function.

The mechanism of renoprotection is still not fully understood, but the main factors probably include:

• improving insulin resistance;

• improvement of endothelial function;

• suppression of inflammatory processes and oxidative stress;

• modulation of AMP-activated protein kinase (AMPK) activity leading to metabolic homeostasis and cellular protection of renal tissue [8–10].

The use of standardized measures of renal function, including eGFR and serum creatinine, which are widely accepted as reliable clinical markers for the early diagnosis of renal dysfunction, ensured the reliability of the results, despite the limitations of the sample and the lack of data on other markers, such as proteinuria.

The present study complements the existing international data and provides valuable information for the Bulgarian outpatient practice, where most patients with T2DM are followed up and treated outside the hospital environment.

A limitation of the study is its single-centre nature and relatively short follow-up period, which

requires confirmation of the results in larger and longer-term studies.

CONCLUSION

The use of metformin in patients with type 2 diabetes mellitus (T2DM) is associated with:

• slower deterioration of renal function;

• reduced risk of developing chronic kidney disease (CKD);

• lower incidence of microalbuminuria.

The results of the present study confirm that metformin not only provides effective glycaemic control, but also performs a key renoprotective function. This is essential for the complex treatment of patients with T2DM in outpatient settings. The inclusion of metformin in the therapeutic regimen may reduce the risk of CKD progression and mortality-related morbidity, contributing to a better clinical outcome and quality of life for patients.

REFERENCES

1. Ekström, N., Schiöler, L., Svensson, A.M., Eeg-Olofsson, K., Jonasson, J.M., Zethelius, B., Cederholm, J., Eliasson, B., Gudbjörnsdottir, S. Effectiveness and safety of metformin in 51,675 patients with type 2 diabetes and different levels of renal function: a cohort study from the Swedish National Diabetes Register. *BMJ Open,* 2012, 2(4), e001076.
2. Wang, H.H., Lin, S.H., Hung, S.Y., Chiou, Y.Y., Hsu, W.C., Chang, C.M., Liou, H.H., Chang, M.Y., Ho, L.C., Wu, C.F., Lee, Y.C. Renal protective effect of metformin in type 2 diabetes patients. *J Clin Endocrinol Metab.* 2025, 110(5), pp. 1224–1234.
3. Ravindran, S., Kuruvilla, V., Wilbur, K., Munusamy, S. Nephroprotective effects of metformin in diabetic nephropathy. *J Cell Physiol.*, 2017, 232(4), pp. 731–742.
4. De Broe, M.E., Kajbaf, F., Lalau, J.D.. Renoprotective effects of metformin. *Nephron,* 2018, 138(4), pp. 261–274.
5. Shen, Y., Cui, J., Yang, R., Shao, W., Yang, J., Wang, B., Pan, B., Zhu, J., Guo, W. Comparison of the 2021 and 2012 CKD-EPI eGFR equations with the 2009 CKD-EPI eGFR equation in a Chinese population. *Kidney Med.*, 2025, 7(9), 101068.
6. Acosta Barrios, A., Goicoechea, M., Verde, E., González-Rojas, Á., Delgado, A., Muñoz de Morales, A., Carbayo, J., Verdalles, U., Pérez de José, A., Luno Fernandez, J. Metformin, a classic treatment for type 2 diabetes with possible renoprotective effects. *Nephrol Dial Transplant.*, 2020, 35(Suppl 3), gfaa142.P0751.
7. Lin, Y.L., Lin, S.H., Wang, H.H., Hsu, W.C, Hung, S.Y., Chiou, Y.Y., Liou, H.H., Chang, M.Y., Ho, L.C., Wu, C.F., Lee, Y.C., et al. Role of metformin in preventing new-onset chronic kidney disease in patients with type 2 diabetes mellitus. *Pharmaceuticals (Basel),* 2025, 18(1), p. 95.
8. Pan, Q., Lu, X., Zhao, C., Liao, S., Chen, X., Guo, F., Yang, C., Liu, H.F. Metformin: the updated protective property in kidney disease. *Aging (Albany NY)*, 2020, 12(9), pp. 8742–8759.
9. Nasri, H., Rafieian-Kopaei, M. Metformin and diabetic kidney disease: a mini-review on recent findings. *Iran J Pediatr.*, 2014, 24(5), pp. 565–568.
10. Rafieian-Kopaei, M., Baradaran, A. Protective effects of metformin on renal tubular cells. *Iran Red Crescent Med J.*, 2014, 16(9), e11662.

ANNUAL OF ASSEN ZLATAROV UNIVERSITY, BURGAS
BULGARIA, 2025, v. LIV(1)

INFLUENCE OF SOME TECHNOLOGICAL FACTORS ON THE QUALITY OF WHITE BRINED CHEESE FROM COW'S MILK

Ruska Nenkova
E-mail: rdnenkova@abv.bg

ABSTRACT

The present study investigated the influence of coagulation temperature, rennet concentration, and calcium chloride ($CaCl_2$) supplementation on the rheological properties and processing performance of white brined cheese produced from cow's milk. Experimental trials were conducted under controlled conditions, and coagulation behaviour was assessed through initial coagulation time (TIC), coagulum compaction time (TCC), and whey drainage time (WDT). The results demonstrated that temperature exerted the strongest effect on gelation, with the most favourable kinetics observed at 35 °C (TIC 14–20 min; TCC 50–58 min). Elevated rennet concentrations (1.0 ml) accelerated coagulation but produced excessively firm and brittle curds, whereas low concentrations (0.2 ml) resulted in weak and unstable gels. Optimal structural properties were obtained with an intermediate dosage (0.5 ml). The addition of $CaCl_2$ at 0.15 ml improved gel strength and reduced coagulation times compared to 0.10 ml, confirming the positive role of ionic calcium in micelle aggregation. WDT trends paralleled TIC and TCC, with balanced syneresis achieved at 35 °C under moderate rennet and $CaCl_2$ levels. Overall, the best technological outcome was achieved with 0.5 ml rennet and 0.15 ml $CaCl_2$ at 35 °C, yielding elastic, dense, and stable curds suitable for high-quality white brined cheese production. These findings highlight the importance of optimizing enzymatic dosage and mineral supplementation in relation to temperature to ensure consistent curd formation and superior cheese quality.

Keywords: *white brined cheese; coagulation temperature; curd rheology; cheese quality*

INTRODUCTION

Milk coagulation by rennet is a crucial stage in cheesemaking, as it determines the structure, yield, and final texture of cheese. The enzymatic activity of chymosin is strongly affected by temperature, with optimal coagulation typically observed between 30–35 °C, whereas higher temperatures reduce enzyme efficiency and lead to excessively firm, brittle gels [1, 2].

The addition of calcium chloride ($CaCl_2$) is also important in cheesemaking, especially when pasteurized milk is used, as it restores ionic calcium levels, enhances micelle aggregation, and shortens coagulation time [3-5]. Another major factor is the concentration of rennet. Increasing enzyme dosage accelerates gelation but often results in firmer, less elastic curds, which may reduce cheese quality [6]. Meanwhile, starter cultures play only an indirect role in coagulation, mainly contributing to acidification and to the development of flavour and aroma during ripening.

Thus, optimization of rennet dosage, $CaCl_2$ addition, and coagulation temperature is essential for achieving desirable rheological properties in white brined cheese.

MATERIALS AND METHODS

Raw cow's milk was analyzed and found to meet EU and BDS standards: titratable acidity – 16 ºT, fat – 3.6 %, density – 1.029 g·cm^{-3}, dry fat-free residue – 8.51 %, total nitrogen – 3.22 %. Microbiological analysis confirmed the absence of *Listeria monocytogenes* and staphylococcal enterotoxins.

A mixed starter (*Lactobacillus delbrueckii subsp. bulgaricus* and *Streptococcus thermophilus*) was used at 0.15–0.2 %. Bovine rennet (strength 1:10,000) was diluted 1:10 prior to use.

Milk (500 ml) was pasteurized (72–74 °C, 10–15 min), homogenized, cooled to target coagulation temperatures, and processed under the conditions shown in Table 1.

Table 1. Experimental conditions for cheese production

Sample	T (°C)	Rennet (ml)	Starter (%)	$CaCl_2$ (ml)
1	30	0.5	0.2	0.15
2	30	1.0	0.1	0.15
3	30	0.2	0.25	0.1
4	32	0.5	0.2	0.15
5	32	1.0	0.1	0.15
6	32	0.2	0.25	0.1
7	35	0.5	0.2	0.15
8	35	1.0	0.1	0.15
9	35	0.2	0.25	0.1
10	40	0.5	0.2	0.15
11	40	1.0	0.1	0.15
12	40	0.2	0.25	0.1

RESULTS AND DISCUSSION

The effects of coagulation temperature, rennet concentration, and $CaCl_2$ supplementation on the rheological parameters of white brined cheese were evaluated through measurements of initial coagulation time (TIC, Fig. 1), coagulum compaction time (TCC, Fig. 2), and whey drainage time (WDT, Fig. 3). The experimental data demonstrate clear trends confirming the strong influence of these technological factors on milk gelation and curd stability.

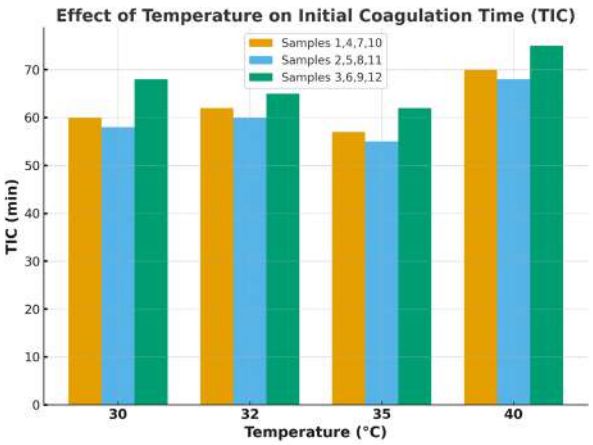

Fig. 1. Effect of temperature and processing conditions on the time of initial coagulation (TIC)

Effect of temperature

Temperature exerted a pronounced impact on coagulation kinetics. At 35 °C (samples 7–9), the shortest coagulation times were observed, with TIC ranging from 14 to 20 min, and TCC completed within 50–58 min. These conditions yielded firm yet elastic curds, indicative of optimal enzymatic activity of chymosin. At lower temperatures of 30–32 °C (samples 1–6), TIC increased slightly (17–22 min), while TCC extended to 50–65 min. The resulting curds were softer and less stable, reflecting slower micelle aggregation. In contrast, at 40 °C (samples 10–12), coagulation was markedly delayed (TIC 23–30 min; TCC 65–74 min), consistent with the reduced efficiency of chymosin at elevated temperatures. The gels produced under these conditions were excessively dense and brittle, suggesting a tendency towards hard and crumbly cheese.

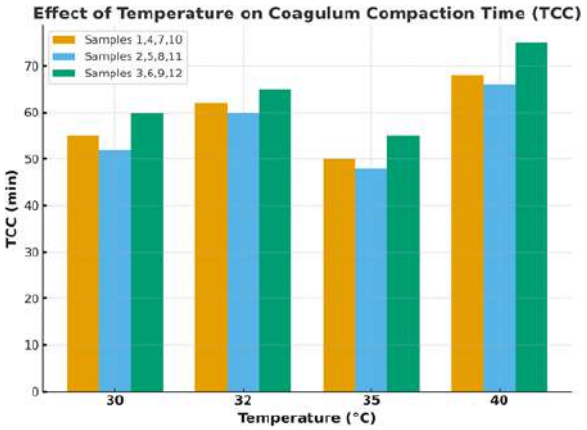

Fig. 2. Effect of temperature and processing conditions on coagulum compaction time (TCC)

Effect of rennet concentration

Rennet dosage was another decisive factor in gel formation. Higher rennet concentrations (1.0 ml; samples 2, 5, 8, 11) consistently shortened TIC and TCC across all tested temperatures. However, the resultant gels were overly firm and brittle, corroborating previous reports that excessive enzyme dosage accelerates gelation but compromises curd elasticity and structural integrity [6]. Conversely, a low rennet concentration (0.2 ml; samples 3, 6, 9, 12) produced weak and unstable coagula unsuitable for firm cheese production. Intermediate rennet levels (0.5 ml; samples 1, 4, 7, 10) achieved a favourable balance, providing adequate gel strength without excessive rigidity.

Effect of calcium chloride

Supplementation with calcium chloride improved both the rate and firmness of coagulation. Samples with 0.15 ml $CaCl_2$ showed shorter TIC and TCC compared to those with 0.10 ml, reflecting enhanced micelle aggregation and gel stability due to elevated ionic calcium levels. These findings are consistent with the literature, where Ca^{2+} is known to enhance enzymatic activity and accelerate casein aggregation [3, 4].

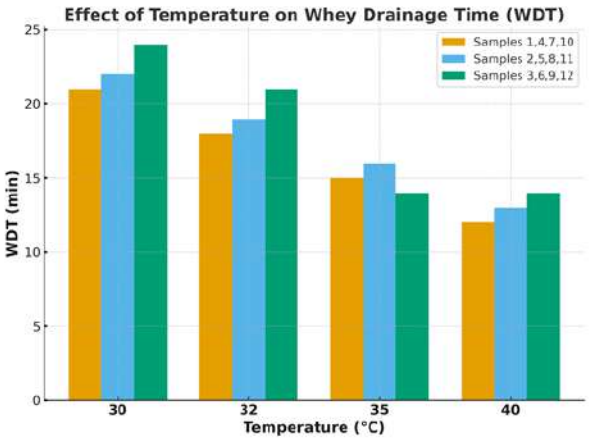

Fig. 3. Effect of temperature and processing conditions on whey drainage time (WDT)

Effect on whey drainage

The whey drainage time (WDT, Fig. 3) exhibited similar trends to TIC and TCC. The most balanced drainage occurred at 35 °C with 0.5 ml rennet and 0.15 ml $CaCl_2$ (sample 7), where WDT was sufficiently rapid to ensure effective syneresis without leading to excessively dry or brittle curds. At lower temperatures (30–32 °C), drainage was considerably slower, resulting in higher residual moisture and weaker curd structure. At 40 °C, WDT was prolonged despite rapid syneresis initiation, likely reflecting impaired curd porosity and reduced whey expulsion due to excessively rigid gel formation.

CONCLUSION

Taken together, the results clearly indicate that coagulation temperature, rennet concentration, and $CaCl_2$ supplementation interact to determine the kinetics of coagulation and curd quality. The most favourable technological conditions were achieved with 0.5 ml rennet and 0.15 ml $CaCl_2$ at 35 °C (sample 7). Under these conditions, the curds exhibited elastic, dense, and stable structures, with optimal coagulation and drainage kinetics suitable for high-quality white brined cheese production.

REFERENCES

1. Johnson, M. E., C. M. Chen, Jaeggi, J. J., Effect of rennet coagulation time on cheese yield and quality, J. Dairy Sci., 2001, 84, pp 1027–1033.
2. Dalgleish, D. G. On the structural models of bovine casein micelles-review and 619 possible improvements. Soft Matter, 2011, 7(6), pp 2265–2272.
3. Lucey, J. A. Formation and physical properties of milk protein gels. J. Dairy Sci., 2002, 85, pp 281–294.
4. McMahon & Oberg Pasta-Filata Cheeses, Chapter 40, Cheese: Chemistry, Physics and Microbiology 2017.
5. Pastorino, A. J., N. P. Ricks, C. L. Hansen and D. J. McMahon, Effect of Calcium and Water Injection on Structure-Function Relationships of Cheese, J. Dairy Sci., 2003, 86, pp 105–113.
6. Walstra, P., Wouters, J. T. M., & Geurts, T. J. Dairy Science and Technology, 2006, CRC Press.

ANNUAL OF ASSEN ZLATAROV UNIVERSITY, BURGAS
BULGARIA, 2025, v. LIV(1)

METHODS FOR MEASURING BLACK CARBON CONCENTRATION IN ATMOSPHERIC AEROSOL

Daniela Ivanova, Gergana Dzhembekova, Stela Naydenova
E-mail: stela.naydenova.eooc@gmail.com

ABSTRACT

Atmospheric pollutants that are hazardous to the environment and human health are measured continuously by monitoring stations. However, some pollutants with high potential risk are not regulated by legislation, and therefore their measurement is not mandatory. One such pollutant is black carbon, which is a component of all atmospheric aerosols. Although its lifetime is only up to two weeks, it has a 460-1500 times stronger warming effect per unit mass than carbon dioxide, which requires rapid measures to limit it. Before implementing such measures, one of the mandatory steps is the selection of appropriate instruments and the conduct of exploratory monitoring. The first data on the concentration of black carbon in Bulgaria was obtained with the Multi-Wavelength Absorption Black Carbon Instrument (MABI) in 2018. The data represented average daily values measured at an urban background station located at the Central Meteorological Observatory of the National Institute of Meteorology and Geophysics. In the city of Burgas, the first studies were in 2020, on the territory of Burgas State University "Prof. Dr. Assen Zlatarov" as part of a project entitled "Study of black carbon and some important hydrocarbons in the atmospheric aerosol in an urban environment" (KP-06-N34/9/19.12.2019).

Key words: *air pollution, black carbon, monitoring, instruments*

INTRODUCTION

Gas emissions and atmospheric aerosols from anthropogenic and natural sources influence global climate change, which in turn poses risks to human health and the environment [1]. Climate policy focuses on decisions and actions regarding carbon dioxide (CO_2), methane (CH_4) and other greenhouse gases which are of particularly important for the processes leading to climate change. These atmospheric compounds are the subject of international targets and agreements. Despite its significant role, black carbon (BC) has been neglected in air quality and climate change decision-making. Only a small number of countries have included black carbon targets in their nationally determined contributions and BC is not part of any climate protocol, revealing a significant gap in strategies [2]. Air quality guidelines focus on fine particulate matter with an aerodynamic diameter of 2.5 μm ($PM_{2.5}$), nitrogen oxides (NO_X), sulphur dioxide (SO_2), and other pollutants to reduce air pollution. The composition of $PM_{2.5}$ varies depending on location and major emission sources, and is primarily composed of sulphates, nitrates, organic compounds, black carbon, and mechanical dust [3]. The World Health Organization (WHO) has emphasized the potential health impacts of particulate matter (PM) and the need for further research, but has not established guidelines for it [4]. Consequently, at national and regional levels, air quality standards do not specifically target BC. Regional treaties, such as the Gothenburg Protocol, recognize BC as a major component of $PM_{2.5}$ but do not require reporting of emissions, and their applicability is geographically limited. Meanwhile, BC emissions are increasing in many places and are not decreasing fast enough in others, despite the availability of fuels and technologies that can lead to rapid reductions [5]. It is technically possible to reduce global emissions by 70% by 2030 relative to 2016 levels.

EXPOSITION

The term "black carbon" was first introduced by T. Novakov in the 1970s [6]. Since then, it has been the subject of continuous research due to its role in atmospheric pollution, which makes it a significant problem, especially in the context of global urbanization. From a chemical perspective, BC is a component of PM known for its strong light-absorbing properties and warming potential,

although it has a relatively short atmospheric lifetime. It is formed during incomplete combustion processes and has a significant impact on regional and global air quality, public health, climate change and ecosystems [7]. After emission, BC mixes with other aerosol chemical compounds, including inorganic ones such as sulphates, nitrates and ammonium, and organic compounds. As a result, BC serves as an important indicator for assessing the adverse effects of particulate matter on human health, especially in environments dominated by combustion sources. BC shows more robust associations with morbidity, mortality, and life expectancy compared to $PM_{2.5}$.

Sources of BC in the atmosphere include forest fires, volcanic eruptions, energy production from the combustion of fossil and biofuels, and certain industrial activities. Today, more than two-thirds of BC emissions are of anthropogenic origin, due to the rapid growth in the consumption of fossil and biofuels by industry and the municipal sector. Natural processes also emit BC into the atmosphere, such as forest and savanna fires. Based on historical BC emission inventories since 1980, the main sources include:

- Combustion of carbon-based fuels, including coal, oil, natural gas, crop residues, and wood for fuel in power plants, industrial facilities, transportation, and residential sectors;
- Gas refining and heating processes;
- Brick production, including material transport, drying the product and kiln firing processes;
- Waste combustion, including municipal and industrial waste;
- Open biomass combustion, including natural fires (forest, grass and peat fires) and human-induced ones (deforestation and open burning of agricultural residues in the field) [8].

Previous studies have shown that domestic heating, household food preparation, diesel vehicles, brick production and forest fires are the most significant sources of BC emissions in the atmosphere.

The spatial distribution of BC air pollution varies across the world, with distinct patterns influenced by regional economic development, regulatory measures, and emission sources. More than 75% of global BC emissions originate in Asia, Africa, and Latin America, mainly due to open biomass burning and residential solid fuel use in developing regions with no comprehensive air quality regulations. China and India top the list of highest national BC emissions. Developed countries, such as the United States, have made substantial progress in reducing anthropogenic BC emissions, mainly from diesel vehicles [9].

In Europe, although specific monitoring of BC in particulate matter is not (yet) mandatory, many air quality monitoring networks measure BC due to its historical association with “black soot”. Proactive countries such as France, having established a national monitoring network of at least 19 BC points across 11 locations by 2021, are leading the way in this regard [10].

Methods for measuring BC in PM

These methods are based on the reflection or transmission of light through PM samples collected over 24 hours on a filter, followed by conversion of optical units to mass-based units [11]. Light is directed onto the filter sample and the amount of light reflected or transmitted is measured. For BC, the amount of light reflected is converted to mass units of PM (OECD standard) (OECD, 1964) or to the black smoke index according to ISO 9835:1993 (ISO, 1993), whereas in the BC method, transmitted light is converted to represent elemental carbon mass. BC measurements has been conducted in Europe since the 1920s, when urban air pollution in many places was dominated by smoke from coal combustion. Although PM determinations are expressed in $\mu g.m^{-3}$, there is no clear relationship with PM mass, as the conversion from optical measurements to mass units depends on location, season, and type of combustion particles.

1. Real-time absorption photometers

These instruments have been available since the 1980s and are based on filter techniques that measure changes in light transmittance at intervals of one to five minutes as particles are deposited on a filter strip [12]. The complex relationship between changes in light transmittance and the absorption and scattering of aerosol on the filter requires adequate calibration of these methods, including selection of an effective wavelength for a valid absorption coefficient, determination of filter spot size, and characterization of aerosol flow. Algorithms have been published to correct for artefactual enhancement of light absorption by filter loading, backscattering, and multiple scattering caused by the BC and filter matrix in conjunction with aethalometers and particle absorption photometers. The polygonal absorption photometer is the only real-time absorption photometer that corrects for these artefacts.

2. Thermo-optical methods

These methods are based on the removal of organic and electrolytic carbon from sampling substrates (e.g., quartz filters) through evaporation and/or combustion at selected temperatures and conversion of the evolved gases into carbon dioxide or methane [13]. This is followed by detection by infrared absorption (CO_2) or flame ionization (CH_4). Elemental carbon is non-volatile and is released only through oxidation.

Most atmospheric organic carbon tends to be released at temperatures of up to 550°C in a pure helium atmosphere, allowing separation from elemental carbon, which is oxidized in 98% helium / 2% oxygen at similar temperatures. Heating in an inert helium atmosphere leads to pyrolysis or charring of some organic carbon compounds, thereby increasing the atmospheric elemental carbon concentrations in the sample. In thermos-optical carbon analysis, this can be corrected by simultaneous measurement of thermal optical reflectance or thermal optical transmittance. Although the principles appear similar, they differ with regards to the location of the temperature monitor (thermocouple) relative to the sample, analytical atmospheres and rates of temperature rise, temperature stages, residence time in each stage, optical pyrolysis configuration, carrier gas flow through the sample, and furnace flushing conditions.

3. Reflectometer

BC/PM_{10} ratios measured with a reflectometer vary considerably across Europe and may largely exceed unity in some locations, as absorption units are converted to BC values in $\mu g.m^{-3}$ using a constant conversion factor [14]. This is a major source of BC, as the highly variable organic carbon/elemental carbon ratio in PM affects absorption due to light scattering due to organic material burning. Typical organic carbon/elemental carbon ratios are around two in urban environments, while organic carbon/elemental carbon ratio may reach five in rural areas with widespread biomass burning. Thus, BC data from different locations, different seasons or long-term series of the same site are not directly comparable. The measurement of BC should always be accompanied by a local calibration of the conversion factor from absorption units to PM values in $\mu g.m^{-3}$ based on the organic carbon/elemental carbon ratio in PM.

4. Polygonal absorption photometer

Currently, this is the only type of real-time absorption photometer designed for BC measurements. It performs real-time light absorption and black carbon measurements using light transmission through a filter, as implemented in the Tricolor Absorption Photometer (TAP) [15]. Based on a decades-proven design that is simple to use and maintain, the TAP measures light absorption at three wavelengths by particles deposited on a filter. By assuming a mass extinction efficiency, the ambient mass loadings of black carbon can also be determined. The TAP has been deployed at Global Aerosol Watch sites around the world for many years, demonstrating good agreement with other concurrently used filter-based light absorption methods.

5. Aethalometer

An aethalometer is a real-time instrument that measures the concentration of light-absorbing particles, such as black carbon (soot), in the air by tracking the darkening of a filter tape as aerosol particles accumulate on it [16]. Aethalometer data can be corrected using published algorithms. The IMPROVE_A protocol in a thermal-optical carbon analyzer equipped with a laser reflectance correction for pyrolyzed organic carbon is currently the most reliable method for measuring organic and elemental carbon concentrations in atmospheric PM. The flexible residence time (150–580 seconds) at each temperature step allows for the measurement of well-defined organic and elemental carbon subfractions, which can be useful in PM source analysis. At its best, during a field campaign, 24-hour BC concentrations by multi-angle absorption photometer and corrected aethalometer data are nearly equal to the 24-hour elemental carbon concentration measured by IMPROVE_A.

Devices used in the territory of Burgas municipality

1. The first BC concentration data for Burgas were obtained using the Multi-Wavelength Absorption Black Carbon Instrument (MABI) for selected months between 2018 and 2021. They represent average daily values measured at an urban background station located at Burgas State University “Prof Dr Assen Zlatarov”. PM samples collected in accordance with EN 12341:2023 were used for BC analysis with the MABI, measuring light absorption at seven different wavelengths. Due to variations in the sources of BC emission, the sampled particles had different densities and masses. Taking these factors into account has also increases the accuracy of the measurements. The data obtained enables the identification of pollution sources across the ultraviolet to infrared spectrum [17|.

2. In the summer of 2021, real-time test measurements were conducted for the first time in the Slaveykov residential area in Burgas using a mobile black carbon device (MA200). The MA200 measures optical attenuation of BC on a filter across five optical wavelengths: infrared, red, green, blue, and ultraviolet (880, 625, 528, 470, and 375 nm, respectively) [18]. The reported detection limit of the MA200 is 30 $ng.m^{-3}$ eBC under a 5 min time base and 150 $mL.min^{-1}$ flow rate, with a resolution of 1 $ng.m^{-3}$.

3. In October 2022, BC measurements were conducted for the first time at an urban background site on the territory of Burgas State University "Prof. Dr Assen Zlatarov" using the Giano BC_1 instrument from DadoLab, acquired under the Blue Growth ColLabs project. Giano Black Carbon is a PM sampler with a built-in BC analyzer, allowing real-time determination directly on the filter during sampling. The instrument can sequentially sample PM with different aerodynamic diameters (2.5 and 10 microns) autonomously for 21 days and is equipped with state-of-the-art data logging solutions. The device can determine the concentration of BC in PM collected on the filter by measuring the laser beam reflection through its optical module [19]. Giano BC_1 is the first solution that uses reflection instead of transmittance to estimate BC. Since October 2022, black carbon concentrations have been analyzed for one month in each of the four seasons.

DISCUSSION AND CONCLUSIONS

Despite extensive efforts over the past 20 years, no generally accepted standard methods exist for measuring BC or elemental carbon in atmospheric aerosol. While most measuring techniques appear to be well correlated, biases in filter-based light absorption and thermal-optical carbon measurements must be identified and corrected to accurately determine aerosol light absorption, BC, and elemental carbon in different environments. Variations in the organic carbon/elemental carbon ratio associated with the bias are due to the absorption of light by filter-based PM, in addition to other artefacts. Current methods for measuring PM and elemental carbon need standardization to facilitate comparison between different study results.

Beginning on January 1, 2026, continuous year-long sampling will be conducted on the territory of Burgas municipality for the first time to determine black carbon concentrations in $PM_{2.5}$.

ACKNOWLEDGMENTS

This study was conducted with financial support from Burgas State University "Prof. Dr. Assen Zlatarov" under contract No. NIH-513/2025.

REFERENCES

1. Ejaz, Z.H., Maya, M.F., Kazim, F., Amir. Ali Z., Akber, Ali N., Khojam A. Impact of climate change and air pollution on cardiovascular disease: A systematic review and meta-analysis protocol. JRSM Cardiovasc Dis., 2025, Sep 29
2. Pittel, K., Ringel, M., Rübbelke, D., Vögele, S., Silina, I. European Climate Policy and the Global Context. In: Lackner, M., Sajjadi, B., Chen, WY. (eds.) Handbook of Climate Change Mitigation and Adaptation. Springer, Cham., 2025.
3. Im, U., Ye, Z., Schuhen, N. et al. Europe will struggle to meet the new WHO Air Quality Guidelines. npj Clean Air 1, 13, 2025.
4. Mallongi, A., Syam, A., Palutturi, S., Madhoun, W. A., Chinwetkitvanich, S., Musadad, D. A., Pathak, S. Health Risk Assessment of NO_2, $PM_{2.5}$ and PM_{10} Exposure in Children and Adolescents, Journal of Human, Earth, and Future, 2025, 6(2), pp. 262–275.
5. Kanaya, Y., Yamaji, K., Miyakawa, T., Taketani, F., Zhu, C., Choi, Y., Komazaki, Y., Ikeda, K., Kondo, Y., Klimont, Z. Rapid reduction in black carbon emissions from China: evidence from 2009–2019 observations on Fukue Island, Japan, Atmospheric Chemistry and Physics, 2020, 20(11), pp. 6339–6356.
6. Novakov, T., The role of soot and primary oxidants in atmospheric chemistry, Science of The Total Environment, 1984, 36, pp. 1–10.
7. Briggs, N., Long, C., Critical review of black carbon and elemental carbon source apportionment in Europe and the United States, Atmospheric Environment, 2016, 144, pp. 409–427.
8. Wang, S., Zhang, M., Zhao, H., Wang, P., Kota, S. H., Fu, Q., Liu, C., Zhang, H., Reconstructing long-term (1980–2022) daily ground particulate matter concentrations in India, 2024, 16, pp. 3565–3577.
9. Ren, Y., Oxford, C.R., Zhang, D. et al. Black carbon emissions generally underestimated in the global south as revealed by globally distributed measurements. Nat Commun., 2025, 16, p. 7010.
10. El. Mehdi EL. Baramoussi, Yangang Ren, Chaoyang Xue, Ibrahim Ouchen, Véronique

Daële, Patrick Mercier, Christophe Chalumeau, Frédéric L.E. Fur, Patrice Colin, Abderrazak Yahyaoui, Oliver Favez, Abdelwahid Mellouki, Nearly five-year continuous atmospheric measurements of black carbon over a suburban area in central France, Science of The Total Environment, 2023, 858(2), 159905.
11. Zhang, Z., Cheng, Y., Liang, L., Liu, J. The Measurement of Atmospheric Black Carbon: A Review. Toxics., 2023, Dec 1;11(12), p. 975.
12. Salo, L., Saarnio, K., Saarikoski, S., Teinilä, K., Barreira, L. M. F., Marjanen, P., Martikainen, S., Keskinen, H., Mustonen, K., Lepistö, T., Aakko-Saksa, P., Hakkarainen, H., Pfeiffer, T., Jalava, P., Karjalainen, P., Keskinen, J., Kuittinen, N., Timonen, H., & Rönkkö, T. Black carbon instrument responses to laboratory generated particles. Atmospheric Pollution Research, 2024, 15(5), 102088.
13. Massabò, D., Prati, P. An overview of optical and thermal methods for the characterization of carbonaceous aerosol. Riv. Nuovo Cim., 2021, 44, pp. 145–192.
14. Yan, B., Kennedy, D., Miller, R.L., Cowin, J.P., Jung, K.H., Perzanowski, M., Balletta, M., Perera, F.P., Kinney, P.L., Chillrud, S.N. Validating a nondestructive optical method for apportioning colored particulate matter into black carbon and additional components. Atmos Environ, 2011, 45(39), pp. 7478-7486.
15. Davies, N. et al., Evaluating biases in filter-based aerosol absorption measurements using photoacoustic spectroscopy, Atmos. Meas. Tech., 2019, 12(6), pp. 3417–3434.
16. Savadkoohi, M., Gherras, M., Favez, O., Petit, J., Rovira, J. et al.. Addressing the advantages and limitations of using Aethalometer data to determine the optimal Absorption Ångström Exponents (AAEs) values for eBC source apportionment. Atmospheric Environment, 2025, 349, 121121.
17. Manohar, M.; Atanacio, A.; Button, D.; Cohen, D., Mabi, A., Multi-Wavelength Absorption Black Carbon Instrument for the Measurement of Fine Light Absorbing Carbon Particles. Atmos. Pollut. Res., 2021, 12, pp. 133–140.
18. Liu, X. et al. Analysis of mobile monitoring data from the microAeth® MA200 for measuring changes in black carbon on the roadside in Augsburg, Atmos. Measure. Tech., 2021, 14, pp.5139–5151.
19. Caponi, L., Cazzuli, G., Gargioni, G., Massabò, D., Brotto, P., Prati, P., A New PM Sampler with a Built-In Black Carbon Continuous Monitor. Atmosphere, 2022, 13, pp. 299–311.

ANNUAL OF ASSEN ZLATAROV UNIVERSITY, BURGAS
BULGARIA, 2025, v. LIV(1)

MOLAR HEAT CAPACITIES OF ALKALI-COBALT DOUBLE SELENATES

Dencho Mihov, Rumyana Yankova, Tsvetelina Yotova,
Victoria Yaneva, Kristian Varbanov
E-mail: denmihov@uniburgas.bg

ABSTRACT

The temperature dependencies of the molar heat capacities of $MeCo(SeO_4)_2$ (Me = Na, K, Rb, Cs) were determined. By statistical manipulation of the obtained values, the parameters in the equations describing these dependencies were determined using the least-squares method. These equations, together with the standard molar entropies, were used to determine the thermodynamic functions $\Delta_0^T S_m^o$, $\Delta_{T'}^T H_m^o$, and $\Phi_m^o + \Delta_0^{T'} H_m^o / T$ for T' = 298.15 K.

Key words: *heat capacity, double selenates, thermodynamic functions*

INTRODUCTION

In nature, selenium occurs in a bound state in the form of selenides, isomorphously or mechanically incorporated into the sulphides of non-ferrous metals. During the pyrometallurgical processing of these ores, selenides are oxidized to selenites and selenates. The recovery of selenium in the gas phase depends on the thermal stability of these compounds. In order to predict the processes occurring in the oxidative roasting of selenide concentrates, it is necessary to have data on the diagnostic characteristics of these compounds: X-ray data, thermal stability, etc.

Many selenates serve as precursors for the preparation of selenides of stoichiometric composition through their reduction with hydrogen or carbon monoxide. In addition, some selenates find application in medicine, agriculture, as well as vitamins for plant nutrition, insecticides for pest control on fruit trees, etc.

For the development of a rational technology for their preparation it is necessary to determine the kinetic parameters of the processes involved. [1] Equally important for the development of a scientifically sound technology is the determination of the thermodynamic properties of these compounds. [2, 3]

Heat capacity is the amount of heat required to change the temperature of the system by one degree.

For the determination of the heat capacity, the following methods are commonly used: the method of ionic increments, the Landy method, and the Einstein and Debye method.

MATERIAL AND METHODS

To obtain the soluble selenates (excluding those of alkali metals), a carbonate, hydroxide or oxide of Me is added to selenic acid. The mixture is heated until the selenic acid is completely reacted. The unreacted oxide, hydroxide or carbonate is removed from the solution by filtration. The resulting solution is concentrated and the crystallised metal selenate is separated from the mother liquor by filtration.

Sparingly soluble selenates are prepared by mixing solutions of particularly pure metal salts and selenic acid. They are thoroughly washed to remove the adsorbed ions, which is monitored by using qualitative reactions with the wash solutions.

The selenates of alkali metals are prepared using alkali bases and selenic acid, the neutral point being monitored using phenolphthalein.

Double selenate salts are prepared from equimolar dilute solutions of the corresponding simple salts. After mixing the solutions in equimolar amounts, the solution is concentrated and the resulting salt is separated by vacuum filtration.

All soluble selenates, including alkali metal selenates, are subjected to double recrystallization at room temperature in a desiccator over concentrated selenic acid.

The synthesized anhydrous selenates are dried at 100ºC and kept in a desiccator until use in calorimetric studies. Selenate crystal hydrates are subjected to dehydration in a crucible heated to appropriate temperatures determined from deri-

vatographic studies. The required temperature is set and maintained by means of a contact thermometer and a relay switch. [4, 5]

It is operated as follows:

Approximately 2 g of selenium crystal hydrate, weighed on an analytical balance to the nearest 0.00004, is poured in a crucible previously heated to constant temperature and placed in a crucible furnace. Using a contact thermometer, the desired temperature is set and the system is plugged into the mains.

After heating for a specified time, the furnace is switched off and the selenium is cooled together with the furnace to 40–50ºC. The crucible is transferred to a desiccator until complete cooling.

The crucible containing the sample is weighed again. The mass difference before and after heating corresponds to the mass loss. [6, 7]

The loss is due to the amount of water separated from the crystal hydrate during dehydration. The dehydration process is carried out repeatedly until the mass change ceases, which is an indication of complete dehydration. A second criterion for completeness of the dehydration is the agreement between the observed mass loss and the theoretically calculated mass loss. [7]

The heat capacities of the selenates were studied using a differential scanning calorimeter (DSC-111, Setaram, France). The scanning conditions were as follows: heating rate 2°C/min in the temperature range 380 – 590ºC, chart speed of 5 mm/min, and amplifier range of 250 V. Heated Al_2O_3 was used as a reference.

The main part of the DSC is a small block of heat-conducting material with two sockets for flat aluminium capsules. The block temperature is increased at a controlled rate. Room temperature is maintained in the outer chamber. Thermocouples located near the working socket are connected in a differential circuit. Any disturbance of the thermal equilibrium in the sockets occurring during the experiment is compensated, and the differential heating power consumption is recorded by a self-recorder as a signal. The sample to be tested is pre-ground into a fine powder and placed into the capsule: a small amount of sample (30 – 70 mg) is required. Heat capacity determination is carried out in three stages:

1. Recording the zero line when the two empty capsules of equal mass are heated.

2. Under the same conditions, recording the curve for the capsule with the sample (Al_2O_3).

3. The same conditions are observed and a record is made when the standard is substituted for the test substance. The second container remains empty.

$$Cp = \frac{I.m'}{I'.m}.Cp_e$$

where: I’ is the distance from the line of the empty capsule to that of the standard (Al_2O_3); I is the distance from the line of the empty capsule to that of the tested substance; m’ is the mass of the standard; m is the mass of the tested substance; and Cp’ is the heat capacity of Al_2O_3 in the tested interval.

RESULTS AND DISCUSSION

The temperature dependence of the heat capacity of a crystalline solid at temperatures higher than 298 K is determined depending on its properties by various equations. The following equation has been adopted in the present study:

$$Cp = a + bT + cT^{-2}$$

It provides the best extrapolation of dependencies at temperatures below and above the investigated temperature range.

Once the temperature dependence of the heat capacity $Cp = f(T)$ is known for a solid, it is possible to determine the thermodynamic functions of the solid in the range from 298.15 K to the melting point. These functions include the entropy (S_T^0), the enthalpy variation ($H_T^0 - H_{298}^0$) and the Gibbs function (ϕ'').

$$S_T^0 = S_{298}^0 + \int_{298}^{T} \frac{Cp}{T} dT$$

$$H_T^0 = H_{298}^0 + \int_{298}^{T} Cp(T)dT$$

$$\phi'' = S_{298}^0 + \int_{298}^{T} \frac{a + bT + cT^{-2}}{T} dT -$$

$$- S_{298}^0 \int_{298}^{T} \frac{a + bT + cT^{-2}}{T} dT$$

The experimental results for the temperature dependence of the isobaric molar heat capacities were obtained following the methodology described by Nazarenko and Ermakov. [8]

The obtained results for the investigated metal selenates and their double salts are presented in tabular form. On the basis of these data, some thermodynamic parameters of the corresponding salts were calculated. The temperature dependences of these parameters are shown graphically in Figures 1 – 4.

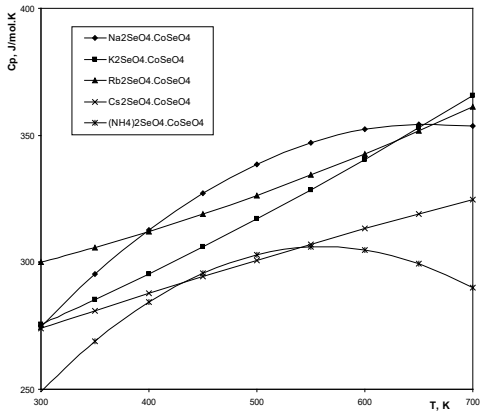

Fig. 1. Calculated values of molar isobaric heat capacities of double selenates $Me_2SeO_4 \cdot CoSeO_4$ (Cp, J/mol.K)

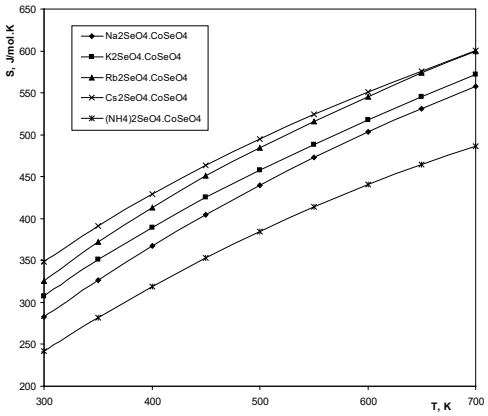

Fig. 2. Calculated entropy values of double selenates $Me_2SeO_4 \cdot CoSeO_4$ (S_T^0, J/mol.K)

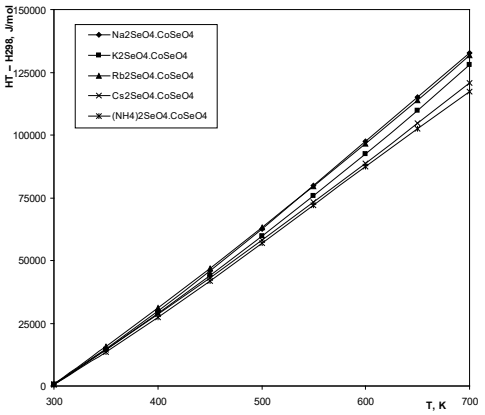

Fig. 3. Calculated enthalpy values of double selenates $Me_2SeO_4 \cdot CoSeO_4$ ($H_T - H_{298}$, J/mol)

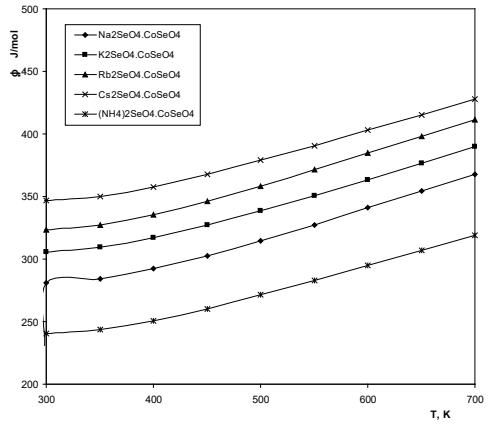

Fig. 4. Calculated Gibbs energy values of double selenates $Me_2SeO_4 \cdot CoSeO_4$ (ϕ'', J/mol)

Table 1. Experimental data on the dehydration of selenate crystal hydrates and their conversion to anhydrous salts

Compound	T °C	$m_{substance}$ to heating	$m_{substance}$ following heating	Loss of mass%	Loss (Theoret. calcul.) %
$Na_2SeO_4 \cdot CoSeO_4 \cdot 4H_2O$	350	4.28363	2.98742	30.26	26.93
$K_2SeO_4 \cdot CoSeO_4 \cdot 6H_2O$	350	4.31548	3.30306	23.46	20.34
$Rb_2SeO_4 \cdot CoSeO_4 \cdot 6H_2O$	350	4.32923	3.43308	20.70	17.32
$Cs_2SeO_4 \cdot CoSeO_4 \cdot 6H_2O$	350	4.34501	3.54378	18.44	15.03

Table 2. Coefficients in the equation describing the dependence of Cp on temperature

Compound	$Cp = a + bT + cT^{-2}$, J/mol.K			$\frac{\delta Cp}{Cp}.10^2$
	a	b	c	
$Na_2SeO_4 \cdot CoSeO_4$	3.7981×10^2	1.3276×10^{-2}	-1.9664×10^7	1.7
$K_2SeO_4 \cdot CoSeO_4$	1.7502×10^2	2.6542×10^{-1}	2.2989×10^6	1.7
$Rb_2SeO_4 \cdot CoSeO_4$	2.6278×10^2	1.3436×10^{-1}	-7.8302×10^5	0.9
$Cs_2SeO_4 \cdot CoSeO_4$	3.3808×10^2	-1.0994×10^{-2}	-7.6781×10^6	1.6

CONCLUSION

Theoretical and experimental investigations of molar heat capacities of double selenates formed from alkali metal selenate and cobalt selenate show good qualitative agreement between model predictions and calorimetric data. The observed deviations arise from the complex crystal structure and specific interactions between alkali cations and Co^{2+} ions. The experimental results contribute to the accumulation of thermodynamic data for this class of compounds and enable more reliable modelling of their thermal properties. This is essential both for fundamental studies of inorganic materials and for potential practical applications related to their thermal stability and functional behaviour.

REFERENCES

1. Godoi Machado R., C. Gaglieri, R. Alarcon, A. Moura, M. Ionashiro, Cobalt selenate pentahydrate: Thermal decomposition intermediates and their properties dependence on temperature changes, Thermochimica Acta, 2020, 689, 178615.
2. Nkhili, N.L., W. Rekik, H. Naïli, A new nickel selenate templated by piperazine: chemical preparation, crystal structure, thermal decomposition, and magnetic properties, Monatsh Chem., 2014, 145, pp. 931–936.
3. Hevroni, L., Z. Shamish, A. Danon, Thermal dehydration and decomposition of copper selenate pentahydrate. J Therm Anal Calorim, 2009, 98(2), pp. 367–370.
4. Spirandeli Crespi, M., C.A. Ribeiro, M. Ionashiro, Studies on double selenates. Thermal decomposition of ammonium selenate and of double selenates of lanthanides, yttrium, and ammonium, Thermochimica Acta, 1994, 239, 157–169.
5. Tankov, I., R. Yankova, D. Mihov, Influence of the coordination metal on the thermal properties of double selenates: Theoretical insights and experimental study, Journal of Molecular Structure, 2023, 1274, 134411.
6. Nabar M.A., S.V. Paralkar, Thermal decomposition of some divalent metal selenates, Thermochimica Acta, 1975, 11(2), pp. 187–196.
7. Nabar, M.A., S.V. Paralkar, Studies on selenates: Thermal decomposition of lanthanum selenate pentahydrate, Thermochimica Acta, 1976, 15(3), pp. 390–392.
8. Nazarenko I.I., A.N. Ermakov, Analytical chemistry of selenium and tellurium. Moscow: Nauka., 1971, p. 251.
9. Kálmán, A., L. Párkányi, G. Argay, Classification of the isostructurality of organic molecules in the crystalline state, Acta Cryst., 1993, B49, pp. 1039–1049.

ANNUAL OF ASSEN ZLATAROV UNIVERSITY, BURGAS
BULGARIA, 2025, v. LIV(1)

SPRING ARRIVAL DATES OF LESSER KESTREL (*FALCO NAUMANNI*) IN BULGARIA

Svetla Dalakchieva, Gradimir Gradev, Stela Naydenova
E-mail: s.dalakchieva@gmail.com

ABSTRACT

Spring migration is among the most climate-sensitive phases of the annual cycle of migratory birds. This study examines the timing of spring arrival of the Lesser Kestrel (Falco naumanni) in Bulgaria, based on both historical records and long-term field observations. Earlier ornithological sources generally indicated arrivals in March and April, whereas recent data from the colony near Levka village (Svilengrad region) demonstrate a marked advancement in arrival dates over the past decade. Between 2014 and 2025, first arrivals shifted from mid-March to late January, representing the earliest records for Bulgaria. The earliest observed arrival was on 12 February 2024 at an average air temperature of 9.9°C, while the lowest temperature at which first birds appeared was 4.6°C in 2023. Analysis revealed two distinct periods: 2019–2021, when first arrivals occurred in early to mid-March, and 2022–2024, when arrivals advanced to early February. These findings indicate a clear phenological shift in the species' migration pattern, strongly associated with increasing winter and early spring temperatures. The results underscore the importance of continuous long-term monitoring and the need to evaluate the effects of climate change on migratory timing and reproductive synchrony in Lesser Kestrel populations in southeastern Europe.

Key words: *Falco naumanni, spring migration, phenology, Bulgaria, climate change*

INTRODUCTION

Spring migration represents one of the most phenologically sensitive processes in birds, responding rapidly to recent climatic changes. Numerous studies have documented a marked advancement in the timing of first arrivals of many migratory bird species, particularly among short- and medium-distance migrants whose migration decisions are closely linked to local temperature conditions in breeding areas [1–3]. Increased mean temperatures during late winter and early spring, along with earlier snowmelt, are identified as key drivers of earlier spring migration [4–5]. However, species-specific responses to climate change vary depending on geographic location, migratory strategy, and breeding phenology [6–7].

The Lesser Kestrel (*Falco naumanni*) is a typical long-distance migrant that winters in sub-Saharan Africa and breeds in southern Europe, including the Balkan Peninsula [8]. It is among the earliest-arriving falcons, and its breeding success is closely tied to synchrony between arrival timing, food availability, and nesting conditions [9]. In the Iberian Peninsula and Italy, several studies report a trend toward earlier spring arrival in recent decades, associated with increasing spring temperatures and shorter winter periods [10].

Despite extensive research on the Lesser Kestrel in southern Europe, data on its spring arrival phenology in Bulgaria remain limited. Most Bulgarian studies have focused on breeding biology, population trends, and nesting habitat selection [11–13], while seasonal dynamics of spring migration and their relationship with climatic variables have received little attention. The present study aims to summarize existing literature and provide new evidence on the spring migration of the Lesser Kestrel in Bulgaria, with particular emphasis on the relationship between first arrival dates, mean spring temperatures, and snow cover conditions.

EXPOSITION

Review of existing data on spring migration of the Lesser Kestrel in Bulgaria

Although the Lesser Kestrel was once widely distributed throughout Bulgaria and bred in close proximity to human settlements, information on its migration remains scarce. Even in foundational works such as *Fauna of Bulgaria* [14], data on the species' migration are limited. Available records

generally indicate spring arrivals in April [15–16]. The species was reported as common in Thrace from April to early October, without details on migration [17], and similarly in the Rose Valley, with arrival in April [18]. Along the Bulgarian Black Sea coast, the species was rarely observed during migration [19]. Nankinov et al. reported spring migration between March and April [20].

In the Red Data Book of Bulgaria, the Lesser Kestrel is described as a migratory species of unknown numbers passing over the country, with post-2000 records concentrated along the Black Sea coast and possibly Eastern Bulgaria [21–24]. According to these sources, the species typically arrives between March and April, with migration occurring from mid-March to early May.

The National Action Plan for the Conservation of the Lesser Kestrel in Bulgaria [23] cites the earliest known migrating individual on 14 March 1988, with northward migration continuing until mid-May. Other early records include a male near Plovdiv on 23 March 1956 [25] and an observation near Slivnitsa (Sofia region) on 26 March 1974 [26]. In northeastern Bulgaria, first returning birds were reported near nests in early April, with breeding pairs established by 5 April 1986 [22]. A single male was observed on 29 March 2014 in Kresna [27], and in the Eastern Rhodopes on 5 April 1986 [28]. Near Mugla village in the Western Rhodopes, a second-year male was recorded on 5 May 2008 [29].

Up-to-date data on spring migration of the Lesser Kestrel in Bulgaria

Long-term observations at the colony in Levka village (Svilengrad region), one of the largest in Bulgaria, provide detailed data on spring arrival. First returning birds were recorded on 18 March 2014 and 5 March 2015 [30-31]. Subsequent years show progressively earlier arrivals: 23 February 2016, 23 February 2017, 24 February 2018, and 22 February 2019. Only in 2020 did the first bird arrive slightly later, on 1 March, but later years set new early arrival records: 11 February 2021, 16 February 2022, and 12 February 2024.

Remarkably, the same ringed female (KZ) was observed in the colony at the end of January in both 2023 and 2025 (26 January 2023 and 29 January 2025), representing the earliest known arrivals for Bulgaria. In Levka, first arrivals are typically adult birds, most often females, followed a few days later by males. The main influx occurs after mid-March, with first-year birds appearing approximately one month later than the earliest adults (Fig. 1.).

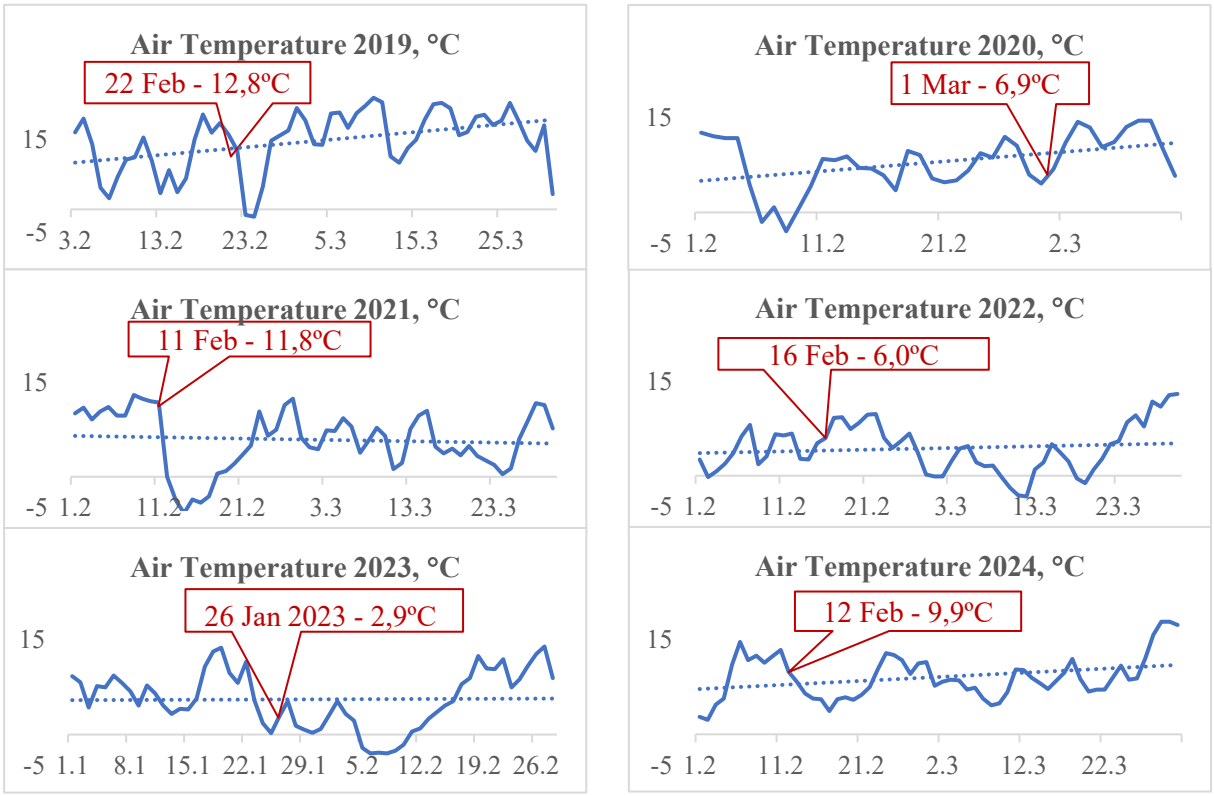

Fig. 1. First arrival date of Lesser Kestrel and air temperature in Levka from 2019 to 2024

DISCUSSION AND CONCLUSIONS

Lesser Kestrel migration follows a classical long-distance pattern, strongly dependent on environmental conditions along the migration route. Recent observations indicate a clear phenological shift, with first arrivals advancing from mid-March to early February. The earliest registration was on 12 February 2024 at 9.9°C, while the lowest temperature recorded for first arrivals was 4.6°C in 2023. These changes suggest a strong correlation between arrival dates and increasing winter and early spring temperatures. Continuous long-term monitoring is essential to assess the impacts of climate change on migratory timing and reproductive synchrony in Lesser Kestrel populations in southeastern Europe.

ACKNOWLEDGMENTS

These results were achieved through Lesser Kestrel Recovery LIFE for Lesser Kestrel LIFE19 NAT/BG/001017 project, funded by the LIFE program of the European Union. The meteorological data were collected within the NIH 472/2022 project.

REFERENCES

1. Lehikoinen, E., Sparks, T.H. & Zalakevicius, M. Arrival and departure dates. Advances in Ecological Research, 2004, 35, pp. 1–31.
2. Rubolini, D., Møller, A.P. & Lehikoinen, E. Intraspecific consistency and geographic variability in temporal trends of spring migration phenology among European bird species. Climate Research, 2007, 35, pp.135–146.
3. Usui, T., Butchart, S.H.M. & Phillimore, A.B. Temporal shifts and temperature sensitivity of avian spring migratory phenology: a phylogenetic meta-analysis. Journal of Animal Ecology, 2016, 86, pp. 250–261.
4. Møller, A.P., Rubolini, D. & Lehikoinen, E. Populations of migratory bird species that did not show a phenological response to climate change are declining. PNAS, 2008,105(42), pp. 16195–16200.
5. Sokolov, L.V. Long-term changes in the phenology of spring migration in the East European Plain. Biology Bulletin Reviews, 2023, 13, pp. 12–27.
6. Both, C. & Visser, M.E. Adjustment to climate change is constrained by arrival date in a long-distance migrant bird. Nature, 2001, 411, pp. 296–298.
7. Jonzen, N., Linden, A., Ergon, T., Knudsen, E., Vik, J. O., Rubolini, D., Piacentini, D., Brinch, C., Spina, F., Karlsson, L., Stervander, M., Andersson, A., Waldenstrom, J., Lehikoinen, A., Edvardsen, E., Solvang, R. & Stenseth, C. Rapid Advance of Spring Arrival Dates in Long-Distance Migratory Birds. Science, 2006, 312, pp. 1959–1961.
8. Cramp, S. & Simmons, K.E. Handbook of the birds of Europe, the Middle East and North Africa. Vol. 2. Hawks to bustards. Oxford University Press. Oxford, 1980, p. 695.
9. Catry, I., Franco, A.M.A. & Sutherland, W.J. Adapting conservation efforts to face climate change: Modifying nest-site provision for Lesser Kestrels. Biological Conservation, 2011, 144, pp. 1736–1743.
10. Rodríguez, C, & Bustamante, J. The effect of weather on Lesser Kestrel breeding success: Can climate change explain historical population declines? J Anim Ecol, 2003, 72, pp. 793–810
11. Gradev, G., Marin, S., Dalakchieva, S., Petrov, R., Vasileva, Y. & Yaneva, S. The abundance and distribution of Lesser Kestrel after restoration in Bulgaria up to 2021. Actas, VIII International Congress on the conservation of the Lesser Kestrel, 2021, pp: 65-67.
12. Gradev, G., Yaneva, S., Bileva, T., Makri, M. & Vlachopoulos, K. Overview of ecosystem services provided by Lesser Kestrel in its main-breeding habitat in Bulgaria. Scientific Papers. Series D. Animal Science. Vol. LXVI, 2023, No. 2, pp. 605-611
13. Yaneva, S., Gradev, G. & Bileva T. Different types of nest boxes used by Lesser Kestrel (Falco naumanni) after being recovered as a breeder in Bulgaria. Scientific Papers. Series D. Animal Science. 2022, Vol. LXV, No. 1, pp. 664– 669.
14. Simeonov, S., Michev, T. & Nankinov, D. Fauna of Bulgaria. Vol. 20. Aves, Bulgarian Academy of Science, Sofia, 1990, pp. 206-208. [in Bulgarian]
15. Patev, P. The birds in Bulgaria. BAS, Sofia, 1950, p. 364. [in Bulgarian]
16. Arabadzhiev, I. Birds of Prey in Bulgaria. Publ. "Science and Art", Sofia, 1962, pp. 1–176. [in Bulgarian]
17. Boev, N., Georgiev, Zh. & Donchev, S. The Birds of Thrace. In: Fauna of Thrace, vol. 1, Sofia. Zoo. Institute with Museum, Bulgarian Academy of Sciences, 1964, pp. 56-105. [in Bulgarian]

18. Donchev, S. The Birds of the Rose Valley. Acta zoologica bulgarica, 1977, 6, pp. 15–34. [in Bulgarian]
19. Donchev, S. Bird migration along the Bulgarian Black Sea coast. Ecology, 1980, 7, pp. 68–83. [in Bulgarian]
20. Nankinov, D., Stoyanov, G., Kouzmanov, G., Todorov, R. Informations sur la situation des rapaces diurnes en Bulgarie. Birds of Prey Bulletin, 1991, 4, pp. 293- 302.
21. Barov, B., Marin, S. & Ivanov, I. Lesser kestrel Falco naumanni Fleischer. In: Golemanski V (ed.), Red data book of Republic of Bulgaria, Bulgarian Academy of Science, MOEW, 2011, 21, 201 5.
22. Iankov, P., Petrov, T., Michev, T. & Profirov, L. Past and present status of the Lesser Kestrel Falco naumanni in Bulgaria. In: Meyburg B-U &Chancellor RD (eds), Raptor conservation today, The World Working Group on Birds of Prey and Owls, Berlin & The Pica Press, London, 1994, pp. 133–137
23. Barov, B. National Action Plan for protection of the Lesser Kestrel (Falco naumanni) in Bulgaria, 2002–2006. - In: Iankov P (ed.), Globally threatened birds in Bulgaria. National Action Plans for their protection. Part 1. Bulgarian Society for the Protection of Birds, Sofia, 2002, pp. 161 –182 [In Bulgarian]
24. Michev, T., Profirov, L., Dimitrov, M. & Nyagolov, K. The birds of Lake Atanasovsko. Status and Checklist. Second Edition, Burgas Wetlands Publication Series, 2004, 5.
25. Kaltschew, B. Zur Kenntnis der Vogelfauna der Umgebung von Plovdiv (Bulgarien). Zool. Abh Ber Mus, Tierk Dresden, 1964, 26, 20, pp. 293–297.
26. Nankinov, D. The Birds of the City of Sofia. Ornithological Information Bulletin, 1982, 12, pp. 1–386. [in Bulgarian]
27. Stoynov, E., Peshev, H., Grozdanov, A., Delov, V., Vangelova, N. & Peshev, D. New data for the presence and numbers of some conservation dependent birds in Kresna Gorge with proposal of original method for individual identification of vultures. Änn. Del Univ. de Sofia "St. Kliment Ohridski", Fac. De Biologia, 2015, 100, 4, pp. 320–331.
28. Yankov, P. Birds of the Eastern Rhodopes. I. Periods of residence and dynamics of the avifauna. Ecology, 1991, 24, pp. 26–43 [in Bulgarian]
29. Daskalova, G, Shurulinkov, P, Stoyanov, G.P. & Borisov, B. Observations of the lesser kestrel (Falco naumanni) in Bulgaria during the period of post-breeding dispersal. Slovak Raptor Journal, 2016, 10, pp. 95–100.
30. Marin, S., Gradev, G. & Kmetov-Biro, E. Action Plan for the Conservation of the Lesser Kestrel (Falco naumanni) in Bulgaria (2021-2030). Green Balkans, Ministry of Environment and Water, Sofia, 2020, p. 82 [in Bulgarian]
31. Touni, S., Todorova, M., Argirova, M., Yaneva, S., Bileva, T. & Gradev, G. Some data about the spring migration of Lesser kestrel (Falco naumanni) in Bulgaria. Scientific conference for students and young scientists "Ecology – a way of thinking", 2022, 14. [in Bulgarian]

ANNUAL OF ASSEN ZLATAROV UNIVERSITY, BURGAS
BULGARIA, 2025, v. LIV(1)

STUDY OF THE SEASONAL EFFECTS ON THE EFFICIENCY OF THE SOLAR INVERTER MODEL FSP 3kVA PLUS

Vasil Ivanov
E-mail: vasil_bi@mail.bg

ABSTRACT

An algorithm was developed to calculate the parameters required for constructing diagrams that reflect the performance of a solar inverter during different seasons. To determine the effective operation of the inverter, the system accounts for the level of solar irradiation at a given moment and records it over a defined period of time according to astronomical seasonal intervals. The recorded monitoring results are visualized through tables and diagrams for a period of one year.

Key words: *FSP 3kVA Plus solar inverter, 24V DC voltage conversion, PWM function, Maximum Power Point Tracking (MPPT) algorithm*

INTRODUCTION

Operation in uninterruptible mode – monitoring

The software of the solar inverter is configured to perform long-term monitoring of the main operating parameters using laboratory loads, including a personal computer, lighting, and an autotransformer.

1. Software settings of the solar inverter according to the hardware technical parameters

The FSP3kVAPlus solar inverter converts a 24V DC voltage supplied by the charge controller into a pure sine wave with a grid frequency of 50Hz and a nominal output power of 3kVA [2, 3].

The embedded Digital Signal Processor (DSP) implements an algorithm for Maximum Power Point Tracking (MPPT), stabilization of the DC voltage from the photovoltaic (PV) modules, and an optimized charge/discharge program for the battery bank (BB).

The inverter software application provides the following functions:

- selection of the priority of the main power source;
- configuration of the charging characteristics according to the type of battery bank;
- definition of the sinusoidal waveform and selection of grid frequency after conversion.

The solar inverter is presented on Fig.1 as a central unit connected to:

- photovoltaic (PV) panels;
- battery bank (BB);
- public low-voltage grid;
- grid-connected consumers.

Fig. 1 Architecture of the solar system with arrows for the directions of the input/output energy exchange

Control screens of the solar inverter

The graphical user interface (GUI), shown in Fig. 2, consists of five sections. The designated fields are configured depending on the battery model, PV panels, and consumer load size:

Field A: Functional menu with management and configuration tools;

Field B: Quick-access menu for frequently used functions;

Field C: Communication port for connection to the inverter as a physical device;

Field D: Monitoring information available to users without administrative rights;

Field E: Main window for real-time monitoring of the solar system, which:

- displays key operating parameters of the solar inverter;
- provides real-time operational information;
- records and stores device data, including nominal and instantaneous performance values.

Fig. 2 Main dialog window of the application for managing and controlling the solar inverter

Energy flow management between sources and consumers

The icons representing the PV panel, battery bank, DC/AC inverter, and loads in Fig. 3 illustrate the system operating in *Power On Mode*.

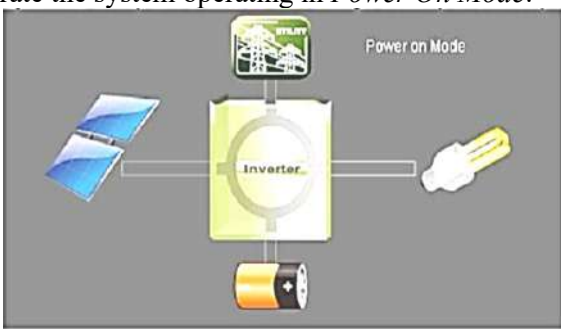

Fig. 3 Part of the application dialog box with the energy sources and the central solar inverter as icons.

By "illuminating" the electrical connections in an energy ring, dynamic changes in energy flow direction are visualized depending on the operating mode.

In *Standby Mode* (Fig. 4), the system demonstrates intelligent energy management from available sources (public grid or PV under sufficient sunlight), through the inverter, to charge the battery bank [1].

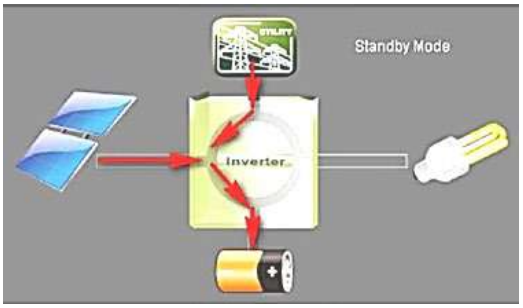

Fig. 4 Additional visualization of the directions of energy transfer under normal operating conditions when the grid is not used as a source

Monitoring parameters of the solar inverter

Fig. 5 presents a record of the instantaneous values of the inverter parameters. The set of monitored parameters is summarized in Table 1.

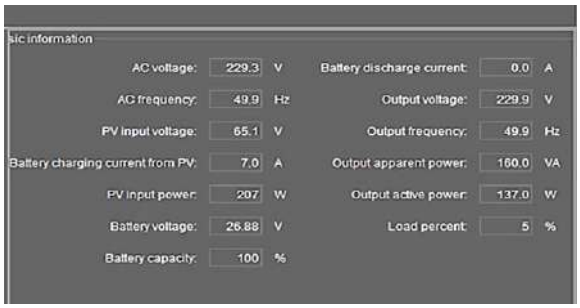

Fig. 5 Record of the current instantaneous values of the solar inverter parameters

Table 1. Set parameters in the solar inverter

Software measurement of output	
Output voltage	230V (constant)
Output frequency	50Hz (constant)
Output apparent	1000VA
Output active power	1000W
Load percent	0 – 100 %
Software-measured of input parameters	
AC voltage	230 V
AC frequency	50 Hz
PV input voltage	30 – 100 V
Battery charging current from PV	max 30 A
PV input power	1108 Wp
Battery voltage	21 – 27V
Battery capacity	30 – 100%
Battery discharge current	max 30 A

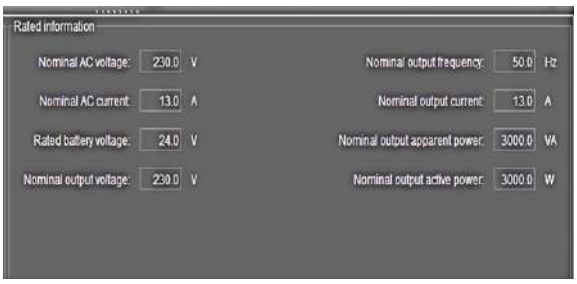

Fig.6. Screen displaying nominal inverter parameters

Basic Operating Modes and Parameter Settings

Functions can be activated or deactivated via the *Enable/Disable* button (Fig. 7) and parameters are configured using the drop-down menus. The settings are saved with the *Apply* button.

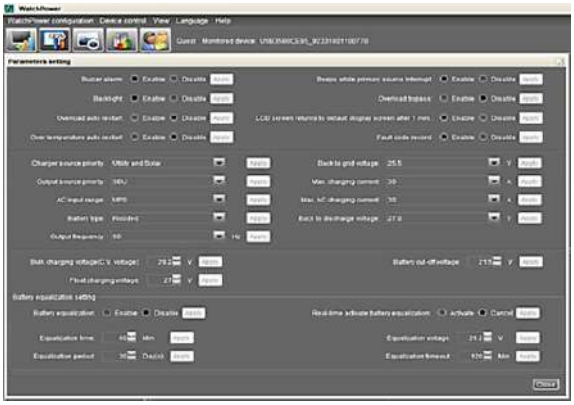

Fig. 7 Screen with parameters settings in operating mode with a 24V BB

The operation of the inverter depends on the selected mode (Fig. 7):

- PV-generated energy primarily charges the battery bank and supplies the inverter, which converts DC to AC for the loads.
- Under cloudy conditions, stored battery energy is automatically used as a secondary source.
- When neither PV nor the battery bank can supply sufficient energy (e.g., at night with discharged batteries), the inverter automatically switches to the public grid within half a cycle (10 ms), ensuring uninterruptible operation and battery recharging.

Additional configurable options include buzzer alarm, backlight, fault recording, etc. (Fig. 7). System settings also allow battery type configuration, bulk and float charging voltages, back-to-grid and back-to-discharge voltages, maximum charging currents (from grid and PV), and output source priority.

For the experiments, the operating mode was set to prioritize PV → Battery → Grid (Solar Battery Utility, or SBU).

RESEARCH METHODS

Visualization of Recorded Monitoring Results via Tables and Charts

- **Computational Methodology**

To determine the effective operation of the solar inverter, the system accounts for solar irradiation levels at a given moment and records them over defined periods of time according to astronomical seasonal intervals [4].

An algorithm was developed to calculate the parameters required for constructing diagrams that reflect the inverter performance across different seasons.

The methodology is based on:

- power generated by PV panels under Standard Test Conditions (STC);
- harvested energy over time;
- efficiency coefficients for power and energy yield;
- seasonal and daily averages of irradiation and inverter output.

Operation of PV solar panels at peak power under Standard Test Conditions (STC) is defined by solar irradiance intensity **G = 1000 W/m^2 , AM = 1.5, t = 25°C**.

$$P_{PV} = (U_{PV})x\,(I_{PV});\ [Wp],. \qquad (1)$$

where U_{PV} is voltage of the PV panel, I_{PV} is current of the PV panel.

Energy generated by the solar panels**:**

$$E_{PV} = (P_{PV})\ x\ (T);\ [kW.h], \qquad (2)$$

where T is the time period [h].

Efficiency coefficient based on the **average power** of the PV panels:

$$\eta_{PV} = \left(\frac{P_{aver.\ PV.}}{P_{inst,\ PV}}\right) x\ (100);\ [\%], \qquad (3)$$

where $P_{avg.PV}$ is the average power delivered by the PV panels [W], $P_{inst,PV}$ is the installed power based on the total capacity of connected consumers [W].

Efficiency coefficient of the PV panels:

$$\eta_{PCП} = \frac{E_{aver.PV}}{E_{inst.PV}} = \left(\frac{(P_{aver.\ meas.})x(T)}{(P_{inst.})x(T)}\right) x(100);\ [\%], \qquad (4)$$

Efficiency of the PV panels under STC conditions:

$$\eta_{PV} = \left(\frac{P_{max}}{(G)x(S_{PV})}\right) x\ (100);\ [\%], \qquad (5)$$

where S_{PV} is the total area of the solar panels (PV) [m^2].

Daily efficiency of the PV panels based on the average annual duration of solar radiation for our latitude, **Tday = 7 hours:**

$$\eta_{day} = \left(\frac{E_{day}}{E_{STC}}\right) x\ (100);\ [\%], \qquad (6)$$

where $E_{day} = (P_{day})x\,(T_{day})$ is the average energy yield Wh, E_{STC} is energy STC.

Power Efficiency Coefficient:

$$\eta_{Pday} = \left(\frac{P_{aver.meas..}}{P_{inst.}}\right) x\,(100);\ [\%], \quad (7)$$

K Energy Harvesting Efficiency:

$$\eta_E = \left(\frac{E_{PV}}{E_{inst.}}\right) x\,(100), [\%]; \quad (8)$$

where:

$$\eta_E = \frac{(P_{aver.\ meas.})x(T)}{(P_{inst.})x(T)} = \frac{E_{PV.}}{E_{inst.}}\ [kWh],\ T = 1\ hour$$

Daily Energy Efficiency of the Solar Inverter:

$$\eta_{E_{day}} = \frac{E_{day}}{E_{inst.day}} = \frac{(P_{aver.\ meas.})x(T)}{(P_{inst.})x(T)} 100; [\%],; \quad (9)$$

where: T_{day} = 7h.

Monthly Average Inverter Efficiency:

$$\eta_{E_{month}} = \left(\frac{\sum_{i=1}^{n} \frac{E_{day}}{n}}{\sum_{i=1}^{n} \frac{E_{inst.}}{n}}\right) x100;\ [\%], \quad (10)$$

where n is the number of days in the month.

Seasonal Energy Efficiency of the Solar Inverter:

$$\eta_{E_{season}} = \left(\frac{\sum_{i=1}^{n} \frac{E_{day}}{n}}{\sum_{i=1}^{n} \frac{E_{inst.}}{n}}\right) x\,(100); [\%], \quad (11)$$

where n is the average number of days in a season (approximately 91 days).

EXPERIMENT

Presentation of Reports from Archived Data by Months and Seasons

Further calculations were performed using daily, monthly, and seasonal data derived from the archived database over one calendar year. Average values of solar irradiation levels, inverter output, and consumed power were extracted from monitoring conducted at *Lukoil-Bulgaria Ltd*.

Based on the monitoring archives, graphs and tables were prepared and distributed by months and seasons. According to the computational methodology algorithm and the monitoring data provided by the solar inverter, calculations were performed for the period from May 2019 to May 2020.

The tabulated data refer to average consumed power *Pavg,meas*, daily solar irradiance levels *G*, and calculated seasonal energy yield *Eseason*. During the experimental process, integral monitoring of the main parameters was applied, as follows:

- **Public electrical grid:** Ugrid and fgrid;
- **Solar panels (PV):** P_{PV} and U_{PV};
- **Battery storage (BS):** U_{BS}, charging current I_{ch}, discharging current I_{dis}, battery capacity C_{BS} in %;
- **Output energy indicators to the loads:** output voltage Uout, output frequency fout, output current Iout, apparent power S_S, active power P_P, and load in %;
- The real-time data measured by the embedded software are recorded in tables for a 24-hour operating mode.

Table 2 presents the average power data calculated for each month from May 2019 to May 2020.

Table 2. Monthly average measured power $\mathbf{P_{aver.meas.}}$ [W] over a one-year period

Month	05. 2019	06. 2019	07. 2019	08. 2019	09. 2019	10. 2019	11. 2019	12. 2019	01. 2020	02. 2020	03. 2020	04. 2020	05. 2020
$\mathbf{P_{aver..meas..}}$	121.8	131	108	127	110	113.8	97.5	123.7	169.9	124.4	107.7	99.2	97.4

In addition to the graphical data for the individual months, May 2020 was included for comparison with the same month of 2019.

Table 3. Seasonal average values for the period May 2019 – May 2020

Season	$\mathbf{P_{aver.}}$, **[W]**	$\mathbf{T_{aver.}}$, **[h]**	$\mathbf{E_{aver.}}$ **[kW.h]**
Spring	126.7	11.2	128.10
Summer	109.5	15.1	148.81
Autumn	120.1	14.5	156.67
Winter	105.9	10.4	99.44

Table 3 presents the average values of the energy generated during the different seasons, as calculated for the period from May 2019 to May 2020.

The data for the average values of power $P_{aver.,meas}$, time T, and energy E are presented for the seasons as follows:

- Winter: 21.12 to 20.03; Spring: 21.03 to 20.06;
- Summer: 21.06 to 22.09; Autumn: 23.09 to 20.12.

The graphical relationship between the power obtained from the PV modules of the solar system over a one-year period and the solar irradiance

measured for the same period are presented in Fig. 8 – 9.

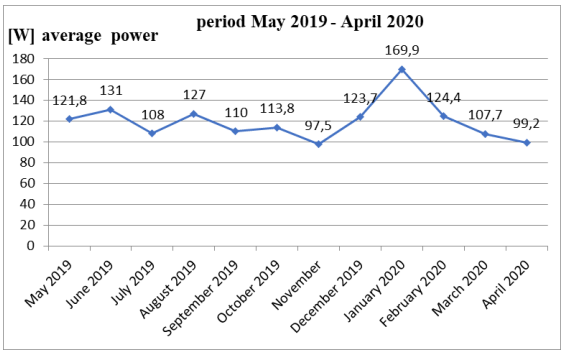

Fig. 8. Monthly average power diagram for a one-year period

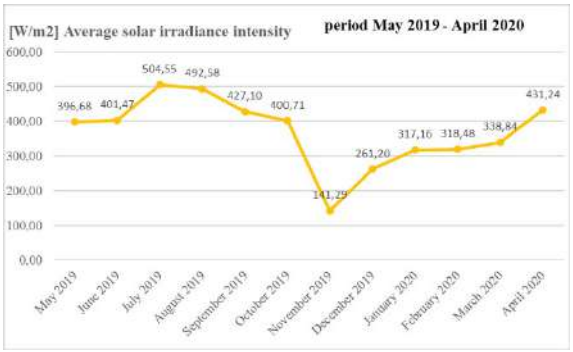

Fig. 9. Average solar irradiance intensity

The graphical representation shows the relationship between the average power levels, the calculated energy values obtained from the solar inverter, and the solar irradiance, all recorded and calculated over a one-year period, and compared by seasons.

The seasonal data for the year were calculated based on the astronomical duration of each season:

- Winter: 21.12 to 20.03; Spring: 21.03 to 20.06;
- Summer: 21.06 to 22.09; Autumn: 23.09 to 20.12.

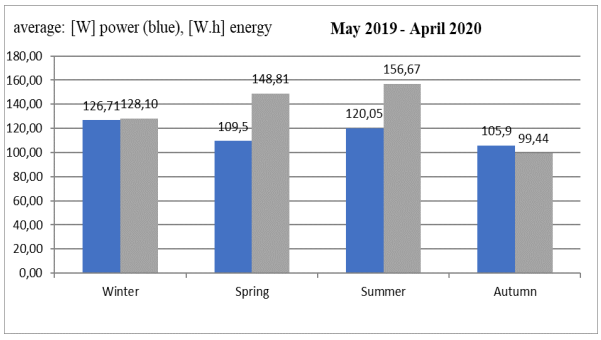

Fig. 10. Monthly average values diagram

CONCLUSIONS

From the graphical presentation of archived data for the main parameters determining inverter efficiency (PV power and solar irradiation), the following conclusions can be made:

- There is a clear correlation between solar irradiation levels, average output power, and harvested energy, strongly influenced by seasonal day length.
- In summer and spring, higher irradiation ensures sufficient energy for uninterrupted inverter operation. In winter, despite lower irradiation, the system shows higher average consumption due to its laboratory usage (lighting and experimental exercises). In this period, daily harvested energy is regarded as savings relative to public grid consumption. January was identified as the month with the highest utilization, while April and November exhibited the lowest.
- There is a direct relationship between average inverter power and the consumed laboratory load. Peaks in power consumption during months with low irradiation were due to increased laboratory usage (lighting, test loading of the system, etc.).
- The analysis demonstrates that a small-scale PV inverter system of up to 3 kW is practically suitable for small houses or holiday cottages, especially during spring and summer, when efficiency is highest and electricity demand is lowest due to the absence of heating loads. Combining such PV systems with small wind generators could further increase efficiency and improve continuity of supply.

REFERENCES

1. Belovski, Iv., Ivanov V., Solar powered thermoelectric cooling system, Annual of Assen Zlatarov University, 2018, Vol. XLVII, Book 1, pp.101–104.
2. Ivanov, V., Research of autonomous low power supply system, Annual of Assen Zlatarov University, 2021, Vol. L, Book 1, pp. 77–81.
3. Ivanov, V., Study of solar voltage inverter model fsp 3kVA, Annual of Assen Zlatarov University, 2023, Vol. LII, pp. 47– 52.
4. Stoyanov, Iv., Ivanov, V., Iliev, T., Ivanov, Hr., Yield and Performance Study of a 1MWp Grid Connected Photovoltaic System in Bulgaria, Journal of Engineering Science and Technology Review , SI, 2020, pp. 206

ANNUAL OF ASSEN ZLATAROV UNIVERSITY, BURGAS
BULGARIA, 2025, v. LIV(1)

POTENTIAL ORGAN-SPECIFIC CARCINOGENICITY OF PORPHYRINS

Yana Koleva
E-mail: *ykoleva@btu.bg*

ABSTRACT

Porphyrin derivatives are found in nature and have important biological roles, such as in light harvesting, oxygen transport, and catalysis. Owing to their intrinsic π-conjugated structure, porphyrin derivatives exhibit characteristic photophysical and electrochemical properties. In biological systems, porphyrin derivatives are associated with various protein molecules through noncovalent interactions. These biologically important roles originate from the functional versatility of porphyrin derivatives. Furthermore, porphyrins are excellent host compounds, forming coordination complexes with various metal ions that add functionality to the porphyrin unit, such as redox activity and additional ligand binding to the central metal ion. The aim of the present work was to predict the possible toxic action (rodent organ-specific carcinogenicity) of porphyrin and its derivatives (chlorin and bacteriochlorin) using the ROSC-Pred software.

Key words: *porphyrin, porphyrin derivatives, toxic action, organ-specific carcinogenicity, predict, software*

INTRODUCTION

In living nature, porphyrins are found in prosthetic groups of proteins and enzymes responsible for the processes of aerobic oxidation, oxygen transport, and peroxide destruction [1–3]. Based on synthetic porphyrins, effective biomimetic catalysts for epoxidation, sulphoxidation, demercaptanization, hydroxylation, carbonylation, and related processes have been developed [2–4]. Despite the great importance of these reactions for chemical industry, synthetic porphyrins have not found significant practical application on an industrial scale. Instead of them, synthetic phthalocyanines, as readily accessible and low-cost analogues of porphyrins, have received widespread application [1].

However, besides synthetic and natural porphyrins, there is another class of these compounds whose applied potential has not yet been fully evaluated. These are the fossil porphyrins (or petroporphyrins) found in heavy oils with high vanadium content. The petroporphyrin content in such fossil raw material can reach 0.1%, which makes heavy oil a promising source for the industrial scale production of petroporphyrins [5].

The porphyrinic macrocycle comprises four pyrrole rings interconnected by methine bridges, forming a planar aromatic system with 22-π electrons, 18 of which are delocalized. This extensive conjugation imparts porphyrins with intense colours and strong absorption in the visible spectrum, contributing to their diverse electronic [6], optical [7, 8], mechanical [9], and chemical [10] properties. At the core, nitrogen atoms create a pocket ideal for coordinating metal ions (e.g., Fe, Co, Mg) in a tetradentate manner [11], enabling charge transfer and reversible electronic changes, such as oxidation or spin state transitions [12].

Porphyrins can be modified at their peripheral α, β, and meso positions, allowing for tailored molecular and crystalline properties, including solubility, reactivity, and photophysical behaviour. Metalloporphyrins, incorporating transition or non-metal ions, can form various metal–ligand complexes with applications spanning biosensors, phototherapy, and catalysis [13, 14].

Due to their unique photophysical and chemical properties, porphyrins are extensively applied in fields such as photoimmunotherapy, photo diagnosis [15], biosensing [16], cancer therapy [17], photocatalysis [18], solar energy conversion [19, 20], chemical sensing [21], optoelectronics [22], molecular recognition [23–25], and the development of new chiral catalysts for asymmetric synthesis [26, 27].

The aim in the present work was to predict the possible toxic action (rodent organ-specific carcinogenicity) of porphyrin and its derivatives (chlorin and bacteriochlorin) using ROSC-Pred.

EXPERIMENTAL

Compound. Porphyrin is a set of heterocyclic macrocycle organic compounds that form four

converted pyrrole subunits connected to their α carbon atoms by methine bridges (=CH–). The resulting structure is highly conjugated, allowing absorption of visible light, and has a central cavity that capable of coordinating with metal ions such as iron or magnesium [28, 29]. Porphyrin derivatives are modified versions of porphyrins, which are large ring-like organic molecules found in nature, such as in heme and chlorophyll. Structural modification provides these derivatives with unique properties that make them useful in various applications, including medicine (e.g, cancer therapy), materials science (e.g., solar cells), and catalysis. The compound names and the structural formulas are presented in Table 1 [28].

Table 1. CAS number, name, and structural formula of porphyrin and its derivatives

No	Name of compound	Structural formula
1	Porphyrin	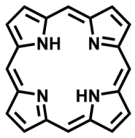
2	Chlorin	
3	Octaethylporphyrin	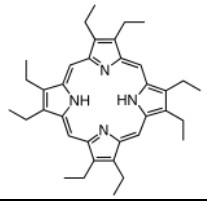

ROSC-Pred. ROSC-Pred is a freely available web service for rodent organ-specific carcinogenicity prediction on the basis of structural formula of organic compounds. The prediction is based on PASS (Prediction of Activity Spectra for Substances) technology and training sets created using data from the Carcinogenic Potency Database (CPDB). CPDB data are available on the EPA Distributed Structure-Searchable Toxicity (DSSTox) Public Database Network [30–32].

P_a (probability "to be active") estimates the likelihood that the studied compound belongs to the sub-class of active compounds (resembles the structures of molecules, which are the most typical in the sub-set of "actives" in the PASS training set).

P_i (probability "to be inactive") estimates the likelihood that the studied compound belongs to the sub-class of inactive compounds (resembles the structures of molecules, which are the most typical in the sub-set of "inactives" in the PASS training set).

Only activities with $P_a > P_i$ are considered as possible for a particular compound.

Applicability domain. The number of new MNA descriptors for a tested molecule may be used for estimation of the applicability domain: the higher the percentage of new MNA descriptors, the less the molecule structure is appropriate for the model. The most accurate predictions are achieved for molecules without new MNA descriptors [31, 32].

RESULTS AND DISCUSSION

In the present work, the ROSC-Pred was used to predict rodent (rat and mice) organ-specific carcinogenicity of the porphyrin and its derivatives. The structure (Porphyrin) lies within the applicability domain. The percentage of new MNA descriptors aws 21.4 % (Pa >Pi). The prediction data for organ-specific carcinogenicity in rats are presented in Table 2, and in mice in Table 3.

Table 2. Prediction of organ-specific carcinogenicity of Porphyrin (rats)

Rats					
Male			**Female**		
Pa	**Pi**	**Organs**	**Pa**	**Pi**	**Organs**
0.585	0.110	Thyroid gland	0.605	0.124	uterus
0.518	0.117	Oral cavity	0.500	0.059	Thyroid gland
0.479	0.122	Ear Zymbals gland	0.490	0.050	All tumor bearing animals
0.461	0.133	All tumor bearing animals	0.579	0.204	Hematopoietic system
0.428	0.156	Spleen	0.513	0.140	Ear Zymbals gland
0.403	0.225	Urinary bladder	0.484	0.192	kidney
0.428	0.306	Hematopoietic system	0.436	0.219	Urinary bladder
0.172	0.121	Maltoni head cancers	0.348	0.162	Small intestine
0.260	0.243	Large intestine	0.262	0.101	Clitoral gland

			0.315	0.244	lung

Table 3. Prediction of organ-specific carcinogenicity of Porphyrin (mice)

Mice					
Male			Female		
Pa	**Pi**	**Organs**	**Pa**	**Pi**	**Organs**
0.816	0.033	Liver	0.886	0.024	liver
0.694	0.104	Stomach	0.778	0.048	Thyroid gland
0.609	0.125	Urinary bladder	0.660	0.100	Stomach
0.615	0.136	Thyroid gland	0.669	0.110	ovary
0.489	0.120	Vascular system	0.611	0.124	Urinary bladder
0.406	0.290	Lung	0.478	0.101	Vascular system
			0.444	0.109	Pituitary gland
			0.413	0.294	Hematopoietic system
			0.177	0.119	Peritoneal cavity

Table 4. Prediction of organ-specific carcinogenicity of Chlorin (rats)

Rats					
Male			Female		
Pa	**Pi**	**Organs**	**Pa**	**Pi**	**Organs**
0.480	0.135	Oral cavity	0.573	0.160	uterus
0.433	0.164	All tumor bearing animals	0.442	0.079	All tumor bearing animals
0.472	0.229	Thyroid gland	0.477	0.165	Ear Zymbals gland
0.398	0.176	Ear Zymbals gland	0.433	0.133	Thyroid gland
0.292	0.236	spleen	0.525	0.276	Hematopoietic system
			0.307	0.222	Small intestine
			0.223	0.147	Clitoral gland
			0.396	0.346	kidney

Table 5. Prediction of organ-specific carcinogenicity of Chlorin (mice)

Mice					
Male			Female		
Pa	**Pi**	**Organs**	**Pa**	**Pi**	**Organs**
0.678	0.074	Liver	0.685	0.068	Liver
0.570	0.167	Stomach	0.696	0.090	Thyroid gland
0.558	0.156	Urinary bladder	0.593	0.116	ovary
0.431	0.173	Vascular system	0.574	0.160	Urinary bladder
0.451	0.215	Thyroid gland	0.521	0.152	Stomach
			0.434	0.119	Pituitary gland
			0.379	0.168	Vascular system

The structure (Chlorin) is also within the applicability domain, with 22.2 % new MNA descriptors (Pa >Pi). The prediction data for organ-specific carcinogenicity of chlorin in rats and mice are presented in Tables 4 and 5, respectively.

The structure (Octaethylporphyrin) lies within the applicability domain, with 19 % new MNA descriptors (Pa >Pi). Prediction data of Octaethylporphyrin for rats and mice are shown in Tables 6 and 7, respectively.

Table 6. Prediction of organ-specific carcinogenicity (rats) of Octaethylporphyrin

Rats					
Male			Female		
Pa	**Pi**	**Organs**	**Pa**	**Pi**	**Organs**
0.317	0.014	Maltoni head cancers	0.533	0.135	Kidney

0.478	0.222	Thyroid gland	0.458	0.096	Thyroid gland
0.423	0.173	Nasal cavity	0.526	0.225	Uterus
0.545	0.316	Kidney	0.444	0.364	Hematopoietic system
0.387	0.217	All tumor bearing animals	0.307	0.229	All tumor bearing animals
0.352	0.225	Oral cavity	0.370	0.302	Ear Zymbals gland
0.310	0.218	spleen			

Table 7. Prediction of organ-specific carcinogenicity (mice) of Octaethylporphyrin

Mice					
Male			**Female**		
Pa	**Pi**	**Organs**	**Pa**	**Pi**	**Organs**
0.715	0.092	Thyroid gland	0.868	0.028	Liver
0.674	0.076	Liver	0.769	0.051	Thyroid gland
0.557	0.112	Lung	0.541	0.195	Urinary bladder
0.521	0.189	Urinary bladder	0.402	0.156	Pituitary gland
0.453	0.255	Stomach	0.365	0.230	ovary
0.359	0.286	Vascular system	0.384	0259	Stomach
			0.276	0.263	Vascular system

CONCLUSION

Porphyrin and its derivatives occur in nature and have numerous applications in various fields. Their toxicological evaluation is of great importance. Various SAR methods have been proposed to reduce the number of animal experiments. Identification of rodent carcinogens remains an important task in the risk assessment of chemicals.

ACKNOWLEDGEMENT

This study was financially supported by Burgas University through the Scientific Research Sector, Project No. 511/2025.

REFERENCES

1. Sorokin, A.B. Phthalocyanine metal complexes in catalysis. Chemical Reviews, 2013, 113, pp. 8152–8191.
2. Nakagaki, S., G.K.B. Ferreira, G.M. Ucoski, K.A.D. De Freitas Castro, Chemical reactions catalyzed by metalloporphyrin-based metal-organic frameworks, Molecules, 2013, 18, pp. 7279–7308.
3. Barona-Castaño, J.C., C.C. Carmona-Vargas, T.J. Brocksom, K.T. De Oliveira, M. Graça, P.M.S. Neves, M. Amparo, F. Faustino, Porphyrins as catalysts in scalable organic reactions. Molecules, 2016, 21, pp. 310.
4. Che, C.-M., J.-S. Huang, Metalloporphyrin-based oxidation systems: From biomimetic reactions to application in organic synthesis, Chemical Communications, 2009, 27, pp. 3996–4015.
5. Tazeev, D., L. Musin, N. Mironov, D. Milordov, E. Tazeeva, S. Yakubova, M. Yakubov, Complexes of Transition Metals with Petroleum Porphyrin Ligands: Preparation and Evaluation of Catalytic Ability, Catalysts, 2021, 11(12), pp. 1506.
6. Saito, S., A. Osuka, E. Vogel, A. Osuka, S. Saito, Expanded Porphyrins: Intriguing Structures, Electronic Properties, and Reactivities, Angewandte Chemie International Edition, 2011, 50, pp. 4342–4373.
7. Tran-Thi, T.H., Assemblies of Phthalocyanines with Porphyrins and Porphyrazines: Ground and Excited State Optical Properties, Coordination Chemistry Reviews, 1997, 160, pp. 53–91.
8. Senge, M.O., M. Fazekas, E.G.A. Notaras, W.J. Blau, M. Zawadzka, O.B. Locos, E.M.N. Mhuircheartaigh, Nonlinear Optical Properties of Porphyrins, Advanced Materials, 2007, 19, pp. 2737–2774.
9. Adinehnia, M., J.R. Eskelsen, K.W. Hipps, U. Mazur, Mechanical Behavior of Crystalline Ionic Porphyrins, Journal Porphyrins Phthalocyanines, 2019, 23, pp. 855–866.
10. Phillips, J.N., Physico-Chemical Properties of Porphyrins, Comprehensive Biochemistry, 1963, 9, pp. 34–72.

11. Biesaga, M., K. Pyrzyńska, M. Trojanowicz, Porphyrins in Analytical Chemistry. A Review, Talanta, 2000, 51, pp. 209–224.
12. Auwärter, W., D. Écija, F. Klappenberger, J.V. Barth, Porphyrins at Interfaces, Nature Chemistry, 2015, 7, pp. 105–120.
13. Brothers, P.J., J.P. Collman, The Organometallic Chemistry of Transition-Metal Porphyrin, Accounts of Chemical Research Journal, 1986, 19, pp. 209–215.
14. Chilukuri, B., U. Mazur, K.W. Hipps, Structure, Properties, and Reactivity of Porphyrins on Surfaces and Nanostructures with Periodic DFT Calculations, Applied Sciences, 2020, 10, pp. 740.
15. Huang, H., W. Song, J. Rieffel, J.F. Lovell, Emerging Applications of Porphyrins in Photomedicine, Frontiers in Physics, 2015, 3, pp. 23.
16. Imran, M., M. Ramzan, A.K. Qureshi, M. Azhar Khan, M. Tariq, Emerging Applications of Porphyrins and Metalloporphyrins in Biomedicine and Diagnostic Magnetic Resonance Imaging, Biosensors, 2018, 8, pp. 95.
17. Tsolekile, N., S. Nelana, O.S. Oluwafemi, Porphyrin as Diagnostic and Therapeutic Agent, Molecules, 2019, 24, pp. 2669.
18. Barona-Castaño, J.C., C.C. Carmona-Vargas, T.J. Brocksom, K.T. de Oliveira, M. Graça, P.M.S. Neves, M. Amparo, F. Faustino, Porphyrins as Catalysts in Scalable Organic Reactions, Molecules, 2016, 21, pp. 310.
19. Li, L.L., E.W.G. Diau, Porphyrin -Sensitized Solar Cells, Chemical Society Reviews, 2012, 42, pp. 291–304.
20. Villari, V., M. Gaeta, A. D'Urso, N. Micali, Porphyrin/Carbon Nanodot Supramolecular Complexes and Their Optical Properties, Colloids Surf. A Physicochemical and Engineering Aspects, 2022, 648, pp.129436.
21. Paolesse, R., S. Nardis, D. Monti, M. Stefanelli, C. di Natale, Porphyrinoids for Chemical Sensor Applications, Chemical Reviews, 2017, 117, pp. 2517–2583.
22. Jurow, M., A.E. Schuckman, J.D. Batteas, C.M. Drain, Porphyrins as Molecular Electronic Components of Functional Devices, Coordination Chemistry Reviews, 2010, 254, pp. 2297–2310.
23. Travagliante, G., M. Gaeta, R. Purrello, A. D'Urso, Recognition and Sensing of Chiral Organic Molecules by Chiral Porphyrinoids: A Review, Chemosensors, 2021, 9, pp. 204.
24. D'Urso, A., N. Marino, M. Gaeta, M.S. Rizzo, D.A. Cristaldi, M.E. Fragalà, S. Pappalardo, G. Gattuso, A. Notti, M.F. Parisi, et al., Porphyrin Stacks as an Efficient Molecular Glue to Induce Chirality in Hetero-Component Calixarene–Porphyrin Assemblies, New Journal Chemistry, 2017, 41, pp. 8078–8083.
25. Gaeta, M., E. Rodolico, M.E. Fragalà, A. Pappalardo, I. Pisagatti, G. Gattuso, A. Notti, M.F. Parisi, R. rrello, A. D'Urso, Self-Assembly of Discrete Porphyrin/Calix[4]Tube Complexes Promoted by Potassium Ion Encapsulation, Molecules, 2021, 26, pp. 704.
26. Bergin, E., Asymmetric Catalysis, Annual Reports on the Progress of Chemistry Section B, 2012, 108, pp. 353–371.
27. Gaeta, M., R. Randazzo, V. Villari, N. Micali, A. Pezzella, R. Purrello, M. d'Ischia, A. D'Urso, A. En Route to a Chiral Melanin: The Dynamic "From-Imprinted-to-Template" Supramolecular Role of Porphyrin Hetero-Aggregates During the Oxidative Polymerization of L-DOPA, Frontiers in Chemistry, 2020, 8, pp. 616961.
28. Mule, J.B., Y. Harangule, S. Deshmukh, S. Bavage, Porphyrin and derivative of porphyrin and its application, International Journal of Research Publication and Reviews, 2022, 3(1), pp. 757-763.
29. ChemIDplus Advanced: https://chem.nlm.nih.gov/chemidplus/
30. EPA Distributed Structure-Searchable Toxicity (DSSTox) Public Database Network-from: (ftp://ftp.epa.gov/dsstoxftp/DSSTox_Archive_20150930/CPDBAS_DownloadFiles/)
31. Way2drug predictive services: http://www.way 2 drug.com/ROSC/index.php
32. Lagunin A., A. Rudik, D. Filimonov, D. Druzhilovsky, V. Poroikov, ROSC-Pred: web-service for rodent organ-specific carcinogenicity prediction, 2017, 34(4), pp. 710-712.

ANNUAL OF ASSEN ZLATAROV UNIVERSITY, BURGAS
BULGARIA, 2025, v. LIV(1)

RESIDUAL STRESSES IN METALS AND ALLOYS AS A FACTOR IN THE STABILITY OF PRODUCTS

Ivan Ivanov
E-mail: ivan_h_ivanov@mail.bg

ABSTRACT

In the present work, the types of internal stresses obtained during the production of parts and structures are presented. The reasons for their occurrence in various technological and production processes have are examined. The stability of residual stresses is investigated, and it is found to depend on the activation energy.

Key words: *residual stresses, stability, activation energy*

INTRODUCTION

Metal products are characterized by the formation of internal stresses as a result of non-uniform plastic, linear or volume deformations occurring within them. The occurrence, distribution and redistribution of residual stresses are always related to the deformation of parts and structures, which determines the mutual position of two points of a metal product, both inside it and on its surface. In the literature, deformations are classified as reversible and irreversible [1, 2]. Reversible deformations are temporary deformations that occur under an external load and disappear after its removal. They are elastic deformations. Irreversible deformations occur under the action of an external load, but do not disappear after the load is removed.

Internal stresses are divided into stresses of the first kind, which are balanced over volumes of the products commensurate with its dimensions. Stresses of the first kind arise as a result of non-uniform force loads or temperature fields. Kind two stresses are equilibrated within microvolumes of the size of the material grains. Stresses of the third kind are balanced within the elementary crystal lattices.

During the production of metal parts, as a result of numerous technological treatments, changes occur in the metal that lead to the formation of stresses [1-4]. In some cases, internal stresses are created intentionally to achieve certain characteristics in parts and structures, and they can be formed in selected areas with specific loading through various technological processes: surface plastic deformation, surface hardening, and chemical-thermal treatment [5-6]. In other cases, residual stresses arise in technological production processes and deteriorate product quality by reducing their stability [7-10].

The purpose of this study is to determine the influence of internal stresses obtained during various technological processes on the reliability of metal products.

RESULTS AND DISCUSSION

The occurrence of internal stresses during various technological processes involved in obtaining and processing blanks is the cause of deterioration of the technical and operational characteristics of finished products. The reliability and operability of a product depend on the quality of the implementation of each technological process.

Metal casting

Uneven cooling of the castings, resistance of the casting mould, differences in the coefficients of thermal expansion in various parts of the casting, variations in wall thickness, phase recrystallization during cooling, and the presence of non-metallic inclusions in the melt affect the size and nature of distribution of internal residual stresses formed during metal casting. Uniform cooling of the mould depends on the shape, dimensions and configuration of the workpieces as well as on the composition of the metal. The temperature field distribution in the metal volume has the greatest influence, and the greatest internal stresses occur in areas with the largest temperature gradient.

The most important stage in foundry production is the cooling of the castings in the mould, as uneven cooling and temperature distribution across the cross-section of the casting cause residual stresses. An incorrect choice of cooling mode

causes part distortion, and when the metal strength is exceeded, hot or cold cracks may appear. The accumulation of internal stresses in the casting reduces the reliability of the product in which it participates, since during operation these stresses can relax, leading to casting distortion and, hence, changes in the mutual arrangement of the connected parts. Moreover, if the stress direction coincides with the operational load direction, a crack may quickly occur due to exceeding the material's failure limit, resulting in product failure. For these reasons, methods to regulate the cooling rate of castings are applied in modern foundry production.

The transition of metal from a plastic to an elastic state has a particularly strong influence on the formation of residual stresses; for cast iron this temperature range is 400-700°C. In practice, metal cooling occurs slowly, and stresses associated with structural inhomogeneity do not have a significant effect, with most of them relaxing during the cooling process.

Metal casting is one of the most common and best-known technological operations for the production of cast iron housing parts, where accuracy and reliability of the manufactured parts depend on shape stability. For example, increased accuracy of products processed on metal cutting machines is a result of the increased accuracy and dimensional stability of both the mechanisms and the machine body. Residual stresses in the bodies of metal-cutting machines cause deformation of guiding components and deterioration of machining accuracy, thereby reducing reliability with respect to the machining accuracy requirements.

Plastic deformation of metals

During plastic deformation processes, such as drawing, rolling, forging, and stamping, inhomogeneity forms in the product cross-section. Under the action of deforming forces, higher stresses arise in surface layers due to the greater deformations that they undergo. Plastic deformation can occur at high temperatures (hot plastic deformation) or at low temperatures (cold plastic deformation). The conditional boundary between the two is the recrystallization temperature, which differs for each metal and alloy. When plastic deformation occurs at temperatures higher than $0{,}4T_L$, it is classified as hot, and at a lower temperature, it is classified as cold.

With regards to the formation of residual stresses during hot plastic deformation, uneven cooling has the strongest influence. However, after hot plastic deformation, the magnitude of residual stresses is significantly lower compared to that produced during cold plastic deformation.

During cold plastic deformation, the occurrence of residual stresses is mainly associated with the formation of multiple defects in the material substructure, such as vacancies, dislocations, and twins. Grain boundaries act as insurmountable barriers to dislocation movements, and these areas become stress concentrators. To overcome the boundary barrier, it is necessary to introduce additional energy into the system, increasing internal stresses. As a result, the mechanical properties of parts improve. Residual stresses can be normal or tangential, depending on the methods of cold plastic deformation and the location of their determination. During cold plastic deformation, residual stresses can be intentionally introduced into selected areas through surface plastic deformation methods, thereby increasing the fatigue durability of products.

Welding

For the most part, welded structures consist of multiple elements joined by welds, with internal stresses arising both during the welding process and during weld cooling being, distributed nonuniformly. The welding sequence and the strength of structural elements significantly affect the magnitude and distribution of welding stresses.

In contrast to the technological processes described above, welding is characterized by local nature of processing. High heating rates to temperatures significantly exceeding the metal melting point cause the occurrence of temperature stresses, structural inhomogeneity in the thermally affected zone, deformations and displacements in structures.

The formation and distribution of welding stresses depends strongly on the power and energy distribution in the heat source, the temperature field, the thermal and structural deformations occurring in the welding process, as well as the rigidity of the material and structure.

For example, in welding steels, the polymorphic transformations of pearlite and ferrite into austenite during heating are accompanied by a decrease in specific volume, while subsequent austenite-martensitic transformation during cooling, causes a significant increase in the specific volume. At the same time, as a result of uneven cooling, the structural changes in the volume of the material do not occur simultaneously, and after cooling, stress distribution is also uneven. The austenite-pearlite transformation in low-carbon steels during cooling takes place at temperatures

below 600°C and its influence on the appearance of residual stresses is relatively small. In alloy steels, due to hindered diffusion mobility of atoms, austenite is stable at lower temperatures when the metal is in the elastic state, and the austenite transformation generates structural-phase residual stresses.

Heat treatment

The formation of residual stresses during heat treatment is associated with the technological processes of hardening, regardless of whether it is surface or bulk. Residual stresses are formed due to uneven temperature distribution, structural transformations dependent on cooling rate, initial temperature and chemical composition. The onset of structural-phase changes during quenching is the main factor that influences total stress, since such changes can reduce thermal stresses until their sign reverses.

Mechanical processing

During mechanical processing of parts, residual stresses arise in their surface layers, caused by the uneven plastic deformation during cutting, local increase in temperature in thin surface layers, as well as temporary phase changes occurring in them. The value and distribution of residual stresses during mechanical processing depend on the processing method, cutting wedge condition, cutting parameters (speed, depth and feed), and cooling quality during the cutting process.

Regardless of the technological reasons for the occurrence of residual stresses, they undergo relaxation over time. This relaxation may be spontaneous, without external influences, or forced, under the influence of heating, or static and dynamic, cyclic and acyclic loads, leading to changes in the geometric dimensions and mutual surface arrangement. In the most general case, the transition of the metal structure from an unstable state to a stable one occurs as a result of the increase in total energy, through the introduction of heat or mechanical vibrations. Thermal energy is transmitted directly from the heating source, while vibrational energy from cyclic loading is dissipated in the product due to the vibration-damping capacity of the material.

During atomic transitions to lower energy states, an energy barrier ΔF_A is overcome, which represents the free energy for activating the reaction:

$$\Delta F = F_1 - F_2 \quad (1)$$

The rate of conversion is determined by thermal fluctuations acting on atoms:

$$V = Cexp\left(\frac{-\Delta F_A}{KT}\right), \quad (2)$$

where: K is Boltzmann's constant, T is temperature, and Cis a constant.

From a thermodynamic perspective, it is convenient to consider the Helmholtz equation, which gives the relationship between internal activation energy ΔU_A, the energy barrier ΔF_A and heat transfer T. ΔS_A:

$$\Delta F_A = \Delta U_A - T\Delta S_A \quad (3)$$

After transforming (2) and (3), the Boltzmann distribution is obtained:

$$V = Aexp\left(-\frac{\Delta U_A}{KT}\right), \quad (4)$$

where: A is a constant accounting for the energy levels.

Therefore, stability corresponds to a structure with increased activation energy.

CONCLUSIONS

Residual stresses formed during the part production are inevitable, and the ability to control their magnitude and direction improves product stability. Their spontaneous relaxation during operation reduces structural stability and can lead to scrapping of the finished product. Control of the magnitude and direction of residual stresses is carried out through appropriate selection of technological processes for obtaining blanks, mechanical and thermal treatment, as well as the correct technological sequencing of assembly, while avoiding the direction of residual stresses in the parts to coincide with the direction of external stresses during their operation.

REFERENCES

1. Birger, I. A. Residual stresses Moscow: Mashgiz, 1963, 232 p. (in Russian).
2. Kolmogorov W., Stresses, deformation, destruction, Metallurgy, 1970, Moscow, 230 p. (in Russian)
3. Hristov St., Deformations, stresses and displacements in welding, Prof. Marin Drinov Academic Publishing House, Sofia 2011.
4. Honeycombe R.W.K., The plastic deformation of metals, 2nd edition, ASM, 1984.
5. Ivanov I., Non-equilibrium structural states of Armco Fe and chrome steels after combined surface plasma-arc and deformational treatment. Varna: Zangador, 2019.

6. Ivanov I., Dikova Ts., Stavrev D., Combined Plasma-Arc Treatment And Surface Plastic Deformation Of Armco-Fe, Advances in Materials and Processing Technologies, Paris, France, October 24th - 27th 2010, AIP Conf. Proc., Volume 1315, pp. 1305–1310.
7. Novoselovic D. et al., Residual stresses in castings produced by press die casting technology, Metalurgija, 2015, 54(1), pp.119–122
8. Nguyen Huu Hai, Zaides S.A., Analysis and selection of a surface plastic deformation method to improve efficiency in strengthening the cylindrical machine parts. BMSTU Journal of Mechanical Engineering, 2025, № 3, pp. 77–85.
9. Zhizhkina N.A., Medvedev A.N. Development of Heat Treatment Technology of Centrifugally Cast Rolls with Working Layer of Chromium-Nickel-Molybdenum Cast Iron. Bulletin of the South Ural State University. Ser. Metallurgy, 2016, vol. 16, no. 3, pp. 83–89. (in Russian)
10. .Ivanov I., Structure of Metals: An Atlas, Varna, Bulgaria, Zangador Research Institute, 2020.

ASSEN ZLATAROV UNIVERSITY
ANNUAL, Vol. LIV, BOOK 1, 2025
TECHNICAL AND NATURAL SCIENCES

Design and layout
Libra Scorp Publisher
www.meridian27.com

Printed in M&BM Ltd.
www.mbm-bg.com

Edition of
Assen Zlatarov University
www.btu.bg

ISSN 2603-3968

BURGAS, 2025

ISSN 2603-3968